Polyphase W-Sn mineralization and rare metal magmatism in relation to the late-Variscan tectono-metamorphic evolution of the southeastern French Massif Central

Matthieu Harlaux, Christian Marignac, Patrick A Carr, Julien Mercadier, Christophe Ballouard, Yujin Jegal, Kalin Kouzmanov, Yann Foucaud, Alfredo Camacho, Jean Cauzid, et al.

▶ **To cite this version:**

Matthieu Harlaux, Christian Marignac, Patrick A Carr, Julien Mercadier, Christophe Ballouard, et al.. Polyphase W-Sn mineralization and rare metal magmatism in relation to the late-Variscan tectono-metamorphic evolution of the southeastern French Massif Central. Mineralium Deposita, 2023, 10.1007/s00126-023-01197-5 . hal-04288010

HAL Id: hal-04288010
https://hal.science/hal-04288010v1

Submitted on 15 Nov 2023

HAL is a multi-disciplinary open access archive for the deposit and dissemination of scientific research documents, whether they are published or not. The documents may come from teaching and research institutions in France or abroad, or from public or private research centers.

L'archive ouverte pluridisciplinaire **HAL**, est destinée au dépôt et à la diffusion de documents scientifiques de niveau recherche, publiés ou non, émanant des établissements d'enseignement et de recherche français ou étrangers, des laboratoires publics ou privés.

Polyphase W-Sn mineralization and rare metal magmatism in relation to the late-Variscan tectono-metamorphic evolution of the southeastern French Massif Central

Matthieu Harlaux[1*], Christian Marignac[2], Patrick A. Carr[2], Julien Mercadier[2], Christophe Ballouard[2], Yujin Jegal[2], Kalin Kouzmanov[3], Yann Foucaud[2], Alfredo Camacho[4], Jean Cauzid[2], and Michel Cuney[2]

[1] BRGM – French Geological Survey, 45060 Orléans, France

[2] GeoRessources, Université de Lorraine, CNRS, 54000 Nancy, France

[3] Department of Earth Sciences, University of Geneva, 1205 Geneva, Switzerland

[4] Department of Geological Sciences, University of Manitoba, Winnipeg, Manitoba R3T 2N2, Canada

* Corresponding author: m.harlaux@brgm.fr

Abstract

The southeastern French Massif Central represents an ideal area to study the linkage between regional metamorphism, crustal partial melting, emplacement of granitic magmas, and hydrothermal Sn-W mineralization in a polyphase tectono-metamorphic setting related to the late-Variscan orogeny. Here, we describe the mineralogical, structural, geochemical, and geochronological characteristics of cassiterite-wolframite-bearing quartz veins at St-Mélany, a small uneconomic Sn-W occurrence located in the North Cévennes area. The veins show evidence of ductile deformation (boudinage, asymmetric folding, dynamic recrystallization) consistent with a synkinematic emplacement during the regional low pressure – medium temperature metamorphism at ca. 320-315 Ma. This dominantly water-fluxed melting event

reaching muscovite-breakdown conditions (T <750°C, P ≈ 0.6 GPa) was synchronous to the emplacement of the syntectonic Rocles peraluminous granite, which is interpreted as a proximal source for the mineralizing fluids at St-Mélany. The U-Pb LA-ICP-MS dating of co-existing wolframite and cassiterite from a mineralized quartz vein yielded lower-intercept ages of 318.4 ± 2.2 Ma and 311.4 ± 1.0 Ma (2σ), respectively. These results suggest a temporal decoupling of W and Sn mineralization with a time gap of 4-10 Myr, but additional work is needed to confirm this interpretation. A weighted mean $^{40}Ar/^{39}Ar$ date of 304.5 ± 4.8 Ma (2σ) was obtained for muscovite from the selvage of a mineralized vein, interpreted as a recrystallization age related to metamorphic re-equilibration or hydrothermal overprinting. Dikes of aplites and pegmatites cut the Sn-W-mineralized veins and were emplaced at 305.9 ± 3.9 Ma (2σ) based on U-Pb LA-ICP-MS dating of magmatic cassiterite. The dikes have highly evolved compositions typical of peraluminous high-phosphorus rare metal granites with Li-F-Ta>Nb-Sn-Be enrichments. Emplacement of the granitic dikes was coeval with the regional low pressure – high temperature metamorphism at ca. 305-300 Ma reaching biotite dehydration-melting conditions (T >800°C, P ≈ 0.4 GPa), which led to the formation of the Velay anatectic dome possibly linked to lower crust granulitization. We conclude that polyphase emplacement of W-Sn-mineralized veins at ca. 320-310 Ma and rare metal granitic dikes at ca. 305 Ma results from contrasting crustal melting conditions, in relation to the late Carboniferous orogenic evolution of the southeastern French Massif Central, and possibly related to delamination of the subcontinental lithospheric mantle.

Keywords

Sn-W mineralization; Rare metal granites; Cévennes; French Massif Central; Variscan belt.

1. Introduction

Hydrothermal Sn-W mineralization is commonly associated with reduced, peraluminous granitoids emplaced in the upper continental crust generating a large variety of ore deposits, including veins, breccias, skarns, and greisens (Černý et al. 2005; Lehmann 2021). Both empirical and experimental studies have shown that Sn and W can be genetically and temporally decoupled during partial melting of metasedimentary protoliths and fluid separation at the magmatic-hydrothermal transition (Romer and Kroner 2016; Yuan et al. 2019; Schmidt et al. 2020; Zhao et al. 2022). Peraluminous rare metal granites and pegmatites, hosting disseminated Li-Ta-Sn-Cs-Be mineralization, have been reported in close spatial association with hydrothermal Sn-W deposits in the European Variscan belt (Cuney et al. 1992, 2002; Breiter et al. 2017; González et al. 2017; Gourcerol et al. 2019; Michaud et al. 2020; Michaud and Pichavant 2020). However, the genetic linkage between these two types of mineralization is commonly obscured by extended metasomatic overprints, ambiguous crosscutting relationships, and the lack of ages for ore minerals, which limit the elaboration of comprehensive metallogenic models.

In Western Europe, the Variscan belt is an important metallogenic province for granite-related Li-Ta-Sn-W deposits (Romer and Kroner 2016; Gourcerol et al. 2019). The French Massif Central (FMC), located within the internal zone of the belt, hosts numerous hydrothermal W±Sn deposits and rare metal granites and pegmatites spatially associated with late Carboniferous peraluminous granitic plutons (Marignac and Cuney 1999; Cuney et al. 2002; Bouchot et al. 2005; Harlaux et al. 2018a,b; Gourcerol et al. 2019). Major peribatholitic wolframite vein-type deposits in the FMC include Enguialès and Leucamp (Lerouge et al. 2007; Lerouge and Bouchot 2009), Puy-les-Vignes (Harlaux et al. 2019, 2021), Echassières (Cuney et al. 1992; Raimbault et al. 1995; Harlaux et al. 2017; Monnier et al. 2019, 2020), and Montredon-Labessonnié (Béziat et al. 1980; Guion et al. 1985). Mining production for W in France was

about 27 kt WO_3 until 1986, and the indicated and measured resources are estimated at about 100 kt WO_3 (Gourcerol et al. 2021). Undiscovered W resources in France are estimated by the BRGM to a potential of about 1 Mt WO_3, including wolframite-bearing vein-type and scheelite-bearing skarn-type deposits (Angel and Bertrand 2018).

Here, we describe the mineralogical, structural, geochemical, and geochronological characteristics of cassiterite-wolframite-bearing quartz veins at St-Mélany located in the North Cévennes area of the southeastern FMC. The St-Mélany occurrence is an ideal natural laboratory to study peribatholitic Sn-W mineralization emplaced during the late-Variscan evolution of the FMC for two main reasons. First, the mineralized veins were emplaced in relation to the well-documented polyphase tectono-metamorphic evolution of a major anatectic domain that is, the so-called Velay dome (Ledru et al. 2001; Brichau et al. 2008; Barbey et al. 2015; Laurent et al. 2017; Villaros et al. 2018). Second, it is the local expression of regional-scale W(-Sn) metallogenic events, also reflected by the occurrence of different types of mineralization, including scheelite-bearing calc-silicate gneisses and wolframite-bearing quartz veins (Noyé 1985; Ramboz et al. 1985; Chauvet et al. 2012; Harlaux et al. 2018a). Thus, the St-Mélany occurrence represents a small-scale example of a polyphase late-Variscan peribatholitic Sn-W vein system, providing an excellent opportunity to decipher the spatial and temporal relationships between the regional magmatic/metamorphic events and the mineralizing processes, and to elucidate the sources of fluids and metals.

2. Geological background

2.1. The North Cévennes area

100 The North Cévennes area is located in the southeastern FMC and consists of three main
101 tectonic-metamorphic series that are structurally from top to bottom (Fig. 1; Marignac et al.
102 1980; Faure et al. 1999, 2001, 2009; Ledru et al. 2001; Barbey et al. 2015; Couzinié et al. 2022):
103 (i) the Joyeuse series consisting of low-grade mica schists and ca. 490-480 Ma old Ordovician
104 orthogneisses that are part of the Lower Gneiss Unit (LGU); (ii) the Cévenole series composed
105 of low- to high-grade mica schists, metagreywackes, quartzites, paragneisses, and calc-silicate
106 gneisses, that are migmatitic in the deepest part of the series, and belong to the Para-
107 Autochtonous Unit (PAU). This structural series represents the lower part of the Cévennes
108 Schist Formation, which continues southward as a stacked kilometer-thick nappe (Arnaud et al.
109 2004); and (iii) the Ardéchoise series that consists of high-grade Cadomian orthogneisses (ca.
110 540 Ma old), including augen gneisses and leucogneisses ("leptynites"; Couzinié et al. 2017).
111 Orthogneisses from the Ardéchoise series are variably migmatitic and are located structurally
112 below the Cévenole series, thus belonging to the PAU (Marignac et al. 1980; Macaudière et al.
113 1987).
114 The metasedimentary rocks of the PAU and LGU were derived from Neoproterozoic to early
115 Cambrian protoliths (ca. 650-550 Ma) deposited along the North Gondwana margin (Melleton
116 et al. 2010; Chelle-Michou et al. 2017; Couzinié et al. 2019) and were intruded by numerous
117 granitoids during the late Carboniferous (330-300 Ma; Brichau et al. 2008; Laurent et al. 2017;
118 Moyen et al. 2017; Villaros et al. 2018). The Cévennes basement records a polyphase tectono-
119 metamorphic evolution including five major events summarized as follows (Aït-Malek 1997;
120 Mougeot et al. 1997; Brichau et al. 2008; Faure et al. 2009; Chauvet et al. 2012; Didier et al.
121 2013; Thierry et al. 2014; Couzinié et al. 2014; Barbey et al. 2015; Villaros et al. 2018).
122 (i) The M1/D1 event (ca. 390-360 Ma) is a high-pressure metamorphic episode
123 (peak conditions of 650-750°C, 1.8-2.0 GPa) resulting from the subduction of oceanic and
124 thinned continental crust domains under the Gondwana (Lotout et al. 2018, 2020). Although

125 records of this event are scare in the studied area, eclogites, granulites, and lherzolites
126 representing exhumed relics of this subduction stage are widespread in the FMC.
127 (ii) The M2/D2 event (ca. 340-330 Ma) corresponds to medium pressure – medium
128 temperature Barrovian metamorphism (700-800°C, 0.8-1.0 GPa) and is associated with the
129 development of regional penetrative foliation S2 and large-scale recumbent isoclinal folds.
130 (iii) The M3/D3 event (ca. 325-315 Ma) consists of north-south compression and low
131 pressure – medium temperature metamorphism (<750°C, 0.5-0.6 GPa), associated with the
132 formation of biotite-bearing metatexites (water-fluxed and muscovite-dehydration melting) and
133 the development of up to kilometer-scale north-verging syn-migmatitic folds. This crustal
134 partial melting event combines north-south shortening and east-west extension and is
135 interpreted to record the flow of the partially melted middle crust (Thierry et al. 2014). There
136 is accordingly a severe decoupling between non-migmatitic and migmatitic domains,
137 underlined by the development of a deformation zone (the so-called "Metamorphic Mylonitic
138 Vellave Zone" of Bouilhol et al. 2006) accommodating the south-verging "normal"
139 displacement of the upper crust relative to the flowing middle crust. This deformation was
140 associated with the emplacement of crust- and mantle-derived magmas, which produced
141 metaluminous to peraluminous porphyritic granites and ultra-potassic mafic magmatic rocks,
142 such as vaugnerites and lamprophyres.
143 (iv) The M4/D4 event (ca. 305-300 Ma) corresponds to late-orogenic northeast-
144 southwest extension and low pressure – high-temperature metamorphism (>800°C, 0.4 GPa),
145 culminating in the development of cordierite±garnet-bearing diatexites (biotite-dehydration
146 melting). This event was synchronous with the emplacement of the Velay anatectic dome,
147 mostly consisting of heterogeneous cordierite-bearing peraluminous granites (CPG in the
148 classification of Barbarin 1999) and diatexites and minor muscovite-bearing peraluminous
149 granites (MPG). Potassium-rich calc-alkaline granites (KCG) and mantle-derived mafic rocks

(lamprophyre, vaugnerite) were mainly intruded during the transition from D3 compression to D4 extension.

(v) The D5 event (ca. 300-295 Ma) is marked by northwest-southeast ductile strike-slip faulting controlling the emplacement of late-orogenic peraluminous granites (e.g., Tanargue, Quatre-Vios) and the opening of Permian intramontane basins (e.g., Prades-Jaujac) accompanying the post-orogenic collapse of the FMC.

2.2. The St-Mélany Sn-W vein system

The St-Mélany Sn-W occurrence (latitude 44°31'33" N, longitude 4°6'50" E) is located in the Drobie valley at about 10 km south of the Velay anatectic dome and about 5 km west of the Mesozoic sedimentary cover (Fig. 1). Other W occurrences are known in the surroundings of St-Mélany, including scheelite-bearing calc-silicate gneisses and wolframite-bearing quartz veins (Noyé 1985; Ramboz et al. 1985). The St-Mélany vein system occurs close to two granitic plutons, the Rocles MPG and the Borne KCG, respectively located about 2 km to the northeast and the west of St-Mélany. The Rocles granite is a syntectonic laccolith composed of a vertical stack of three main intrusive units (biotite-rich, biotite-muscovite, and muscovite-rich), which are dated at 325 ± 4 Ma, 318 ± 3 Ma, and 324 ± 4 Ma, respectively (electron microprobe U-Th-Pb monazite ages; Be Mezeme et al. 2006, 2007). These chemical dates are consistent with a U-Pb zircon concordia age of 319.8 ± 3.8 Ma obtained on the muscovite-rich Rocles granite (Couzinié 2017) that constitutes the uppermost part of the pluton. The Borne pluton consists of a K-feldspar megacrystic biotite ± amphibole-bearing monzogranite (KCG type) representing the eastern extension of the Pont-de-Montvert pluton, which is left-laterally offset to the south by the Villefort strike-slip fault (Mialhe 1980). Anisotropy of magnetic susceptibility studies showed that the Pont-de-Montvert-Borne pluton is characterized by a well-developed east-

175 west-trending magnetic lineation, which is interpreted to record emplacement of the granitic
176 stock during late-orogenic extension (Talbot et al. 2004). This is consistent with the east-west
177 subvertical magmatic foliation marked by the alignment of K-feldspar megacrysts and
178 schlierens in the Borne granite (Mialhe 1980). Geochronological data for the Pont-de-Montvert-
179 Borne pluton range between 309.7 ± 3.6 Ma (U-Pb zircon; Couzinié 2017), 303 ± 3 Ma (U-Pb
180 monazite; Brichau et al. 2008), and 302.5 ± 0.9 Ma (U-Pb zircon; Laurent et al. 2017). Note
181 that the Largentière granite, interpreted as a satellite extension of the Borne granite to the east,
182 is dated between 304.1 ± 6.3 Ma (U-Pb zircon; Couzinié et al. 2014) and 298.9 ± 1.8 Ma (U-
183 Pb zircon; Laurent et al. 2017).
184 The Sn-W mineralization at St-Mélany is hosted by a northeast-trending vein system (Fig. 2a)
185 that was emplaced in cordierite-biotite-bearing mica schists of the Cévenole series, close to the
186 chlorite- isograde (Fig. 1). The veins mainly consist of quartz with sporadic presence of
187 cassiterite and wolframite as well as variable amounts of tourmaline, pyrite, arsenopyrite,
188 chalcopyrite, muscovite, albite, apatite, and beryl. The cassiterite and wolframite mineralization
189 occurs solely at the hanging wall and footwall of the quartz veins close to the contact with the
190 mica schists (Fig. 2b). Tourmalinization is the dominant hydrothermal alteration at St-Mélany,
191 and tourmaline occurs as pervasive replacements along the schistosity planes of the mica schists
192 and as veins crosscutting the metamorphic foliation (Noyé 1985; Harlaux 2016).
193 The vein system is cut by northeast-striking dikes of aplites and pegmatites (Fig. 2c) dated at
194 306.5 ± 3.1 Ma ($^{40}Ar/^{39}Ar$ muscovite plateau age; Chauvet et al. 2012). A swarm of northeast-
195 trending lamprophyre dikes cuts the vein system (Fig. 2d) and was likely emplaced during the
196 regional mantle-derived mafic magmatism at ca. 305 Ma (Couzinié et al. 2014; Barbey et al.
197 2015; Laurent et al. 2017). About 4 km southwest of St-Mélany, a similar lamprophyre dike
198 crosscutting the low-grade mica schists of the Cévenole series was dated at 306.6 ± 2.4 Ma (U-
199 Pb zircon; Laurent et al. 2017). This lamprophyre is located 10 km east of the contact with the

Borne porphyritic granite and is part of a dike swarm in proximity to St-Jean-de-Pourcharesse (Weisbrod et al. 1974). Vaugnerite dikes, i.e., potassic plutonic rocks equivalents to lamprophyres (see Moyen et al. 2017), were emplaced in migmatitic gneisses of the Ardéchoise series at 306.6 ± 1.6 Ma at Loubaresse, 305.9 ± 1.7 Ma at Meyras, and 306.1 ± 1.3 Ma at Pont-de-Bayzan (U-Pb zircon; Laurent et al. 2017), located about 10-20 km north from St-Mélany. Late quartz-barite veins and silicified breccia zones with an east-west orientation cut the Sn-W-bearing quartz veins (Fig. 2e). These vein-breccia bodies show crack-and-seal textures with open-space geodic infill and host a galena-sphalerite mineralization. They represent the last hydrothermal event known at St-Mélany and were likely emplaced during the Triassic – Lower Jurassic extension, as other similar Pb-Zn(-Ba) occurrences around the Borne pluton (Mialhe 1980) and in the Largentière basin southward (Aquilina et al. 2011), as well as numerous F-Ba deposits in the whole FMC (Marcoux et al. 1990; Sizaret et al. 2004, 2009).

3. Analytical methods

3.1. Petrography and geochemistry

Mineralogical analyses were carried out at GeoRessources (Université de Lorraine, France) using an Olympus BX51 optical microscope and a JEOL J7600F scanning electron microscope (SEM) equipped with a SDD-type energy dispersive X-ray spectrometer (EDS) coupled to an Oxford Wave wavelength dispersive X-ray spectrometer (WDS). Backscattered electron (BSE) and cathodoluminescence (CL) images were acquired on carbon-coated polished thin sections with an accelerating voltage of 15 kV. Major and minor element compositions of minerals were measured using a Cameca SX100 electron microprobe analyzer (EMPA) equipped with five WDS spectrometers at GeoRessources. Measurements were performed with a 15 kV

225 accelerating voltage, a 20 nA beam current, and a focused beam of 1 µm. Standards used for
226 calibration were scheelite (W), cassiterite (Sn), albite (Na, Si), lithium tantalate (Ta), lithium
227 niobate (Nb), forsterite (Mg), corundum (Al), orthoclase (K), andradite (K, Fe), pyrophanite
228 (Ti, Mn), apatite (P), barite (Ba) and pure scandium (Sc). The intensities of 16 elements were
229 acquired at Kα lines of Na, Mg, Al, Si, P, S, Ca, Sc, Ti, Mn, Fe, and Lα lines of Ta, W, Sn, Nb
230 with a 10 s on-peak acquisition time.
231 The µXRF maps were acquired using a Bruker Tornado M4 benchtop spectrometer at
232 GeoRessources. The instrument is equipped with a Ag-anode and two XFlash 430 ® SDD
233 detectors of 145 eV energy resolution at the Mn Kα line. The primary X-ray beam was set to
234 150 µA and 50 kV to ensure a dead time below 20% on all mineral phases. The beam was
235 focused with polycapillary optics to a 20 µm size on the sample using a 30 µm pixel size. The
236 dwell time per pixel was 10 ms. A full XRF spectrum was recorded in each pixel with an energy
237 gain of 0.01 keV per channel. XRF data cubes were processed using PyMCA (Solé et al. 2007)
238 to decompose XRF spectra and remove spectral interferences as much as feasible. Despite
239 spectral decomposition, some interferences were not fully solved, such as Ca-Kα (3.69 keV)
240 and Sn-Lβ (3.66 keV) lines in cassiterite and Ta-Lβ (8.15 keV) and W-Lβ (8.39 keV) lines in
241 wolframite.
242 Whole rock geochemistry was performed at the SARM-CNRS (Vandoeuvre-lès-Nancy,
243 France). Samples of 5-10 mg crushed to <80 µm were prepared and melted using a
244 $LiBO_2$+H_3BO_3 alkaline flux, excepted for Li, B and F. After quenching, samples were
245 dissolved in an acid solution (HNO_3+HF) for complete digestion. Major elements were
246 measured with a Thermo Fisher ICap 6500 ICP-OES, and minor and trace elements with a
247 Thermo Fisher X7 quadrupole ICP-MS, following the procedure of Carignan et al. (2001). For
248 B, powders were melted using Na_2CO_3 and analyzed by absorptiometry (Agilent CARY60)
249 following ion exchange chromatography. Lithium was measured by flame atomic absorption

spectrometry (AAS, Agilent 240FS) after sample dilution in HF + $HClO_4$. Fluorine was analyzed by potentiometry after melting using Na_2CO_3 flux and filtration.

3.2. U-Pb geochronology

In situ U–Pb isotopic analyses of wolframite and cassiterite were performed at GeoRessources using a Nu Instruments AttoM^{TM} ES sector field - inductively coupled plasma - mass spectrometer (SF-ICP-MS) coupled to an ESI 193 nm, ArF excimer laser ablation system with a two-volume HelEx sample cell. Ablation occurs in a He environment (flow rate between 615 and 700 mL/min) within the sample cell and is then mixed with N_2 at a flow rate of 3 mL/min. An Ar makeup gas with a flow rate of between 330 to 400 mL/min is added following the N_2 and before entering a gas mixing bulb and then the ICP torch. Gas flow rates and ion lens parameters were optimized on the NIST-612 reference glass material in raster mode to provide the highest sensitivity, maintain low oxide levels and minimize the fractionation of Th/U. The ThO/Th ratio was below 0.05% and the Th/U ratio was typically from 0.9 to 1.0. Vein-hosted wolframite and cassiterite were analyzed during a single session with a spot size of 90 µm, energy density of 4 J/cm^2, and a repetition rate of 6 Hz. Pegmatitic cassiterite was analyzed during a different session with spot sizes of 60 and 45 µm, energy density of 4 J/cm^2, and a repetition rate of 6 Hz. For all sessions, the targeted area was pre-ablated with 5 pulses of a larger and less energy dense (2 J/cm^2) laser spot to remove any surficial Pb contamination. Each measurement consists of 40 s analysis and 20 s each of pre- and post-ablation background washout time.

The following isotopes were measured (integration time in parentheses): ^{202}Hg (500 µs), ^{204}Pb (500 µs), ^{206}Pb (500 µs), ^{207}Pb (1.5 ms), ^{208}Pb (500 µs), ^{232}Th (500 µs), ^{235}U (500 µs), and ^{238}U (500 µs) resulting in a sweep of all isotopes in 167 ms. The sensitivity of the LA-SF-ICP-MS

on ^{238}U was quantified with the NIST-614 reference glass material and was between 1.18 x 10^4 (45 μm spot size) and 5.0 x 10^4 (90 μm spot size) counts per second dependent on the analytical conditions employed. Uranium, Th, and Pb concentrations were determined after normalizing measured cps for each analyte to the NIST-614. Due to the different matrices between the NIST-614, wolframite, and cassiterite, these concentration values are considered as semi-quantitative (Jochum and Stoll 2008). U–Pb isotopic ratios were corrected for background signal, downhole fractionation, instrument drift, and instrument mass bias in the IoLite™ 4 program using the UComPbine data reduction scheme (Paton et al. 2011; Chew et al. 2014). Details on the analytical procedure for LA-ICP-MS analysis of wolframite are given in Carr et al. (2021). U-Pb ratios of wolframite were normalized to an internal reference material from the Maoping deposit, China (14-MP-28 from Legros et al. 2020; ID-TIMS U-Pb age of 158.47 ± 0.63 Ma; unpublished data). Two other wolframites from the Mount Carbine deposit, Australia (PB_MC; unpublished U–Pb age of 279.4 ± 1.0 Ma) and Yaogangxian W deposit, China (YGX-2113; ID-TIMS U–Pb age of 160.9 ± 0.2 Ma; Yang et al. 2020) were analyzed for quality control (ESM Table S4). The U-Pb ratios of cassiterite were normalized to the Yankee cassiterite assuming a U–Pb age of 246.48 ± 0.51 Ma (Carr et al. 2020). The $^{207}Pb/^{206}Pb$ ratios of both wolframite and cassiterite were normalized to the NIST-614 synthetic glass, assuming a value of 0.8710 ± 0.0008 (Woodhead and Hergt 2001). The Jian-1 cassiterite (U–Pb age of 154.969 ± 0.082; Tapster and Bright 2020) was analyzed for quality control of cassiterite ages (ESM Table S4).

The long-term reproducibility ('excess variance') of U-Pb ages of this LA-ICP-MS system is estimated to be 1.9% using the variance of the U-Pb age of the Jian-1 cassiterite (Carr et al. 2022). In the absence of wolframite long-term U-Pb age reproducibility, we assume the same value as used for cassiterite. U-Pb ages of wolframite and cassiterite are reported at two uncertainty levels following the guidelines of Horstwood et al. (2016). The first and lesser

uncertainty represents the 95% confidence interval of the lower intercept age, and the second (in parentheses) and larger uncertainty includes the excess variance added in quadrature.

3.3. $^{40}Ar/^{39}Ar$ geochronology

$^{40}Ar/^{39}Ar$ analytical work was performed at the University of Manitoba (Canada) using a multi-collector Thermo Fisher Scientific ARGUS VI mass spectrometer linked to a stainless steel Thermo Fisher Scientific extraction/purification line, Photon Machines (55 W) Fusions 10.6 CO_2 laser, and Photon Machines (Analyte Excite) 193 nm laser. Argon isotopes (from mass 40 to 37) were measured using Faraday detectors with low noise 10^{12} Ω resistors, and mass 36 was measured using a compact discrete dynode (CDD) detector. All specimens (sample and standard) were irradiated for 17 hours in the Cd-lined, in-core CLICIT facility of the TRIGA reactor at the Oregon State University, USA. Standard of Fish Canyon sanidine (Kuiper et al. 2008) was placed in a Cu sample tray, with a KBr cover slip, in a stainless-steel chamber with a differentially pumped ZnS viewport attached to a Thermo Fisher Scientific extraction/purification line and baked with an infrared lamp for 24 hours. Unknowns consist of discs of 5 mm in diameter and ~150 μm thick that were cut from a thick polished section investigated by optical microscopy and SEM prior to $^{40}Ar/^{39}Ar$ analyses. The discs were mounted using a ceramic adhesive (PELCO) on a quartz slide placed in a stainless-steel chamber with a sapphire viewport attached to the same stainless-steel high vacuum extraction system as the CO_2 laser and baked with an infrared lamp for 48 hours.

For this study, a raster size of about 100 x 100 μm was used, and ablation pits were excavated to an estimated depth of ~50 μm. Measured isotope abundances were corrected for extraction-line blanks, which were determined before every sample analysis. Line blanks in both the Excimer and CO_2 system averaged ~3 fA for mass 40 and ~0.013 fA for mass 36. Detector

intercalibration (IC) between the different faraday cups was monitored (in Qtegra) every four days by peak hopping ^{40}Ar. Calculated values are ICH1: 1.0000, ICAX: 1.0745, ICL1: 1.0637, and ICL2: 1.0534, with an error of ~0.2%. The IC factor between H1 and the CDD was measured using 70 air aliquots interspersed with the unknowns resulting in ICCDD value of 1.0081 ± 0.0002 per amu. A value of 295.5 was used for the atmospheric $^{40}Ar/^{36}Ar$ ratio (Steiger and Jäger 1977) for the purposes of routine measurement of mass spectrometer discrimination using air aliquots and correction for atmospheric argon in the $^{40}Ar/^{39}Ar$ age calculation. Corrections were made for neutron-induced ^{40}Ar from K, ^{39}Ar and ^{36}Ar from Ca, and ^{36}Ar from Cl (Renne et al. 1998; Renne and Norman 2001). Data collection, reduction, error propagation, and age calculation were performed using the MassSpec software (v.8.091; Deino 2013) and the decay constants recommended by Steiger and Jäger (1977).

4. Results

4.1. Structural and paragenetic features of the mineralized veins

The St-Mélany system mainly consists of subhorizontal quartz veins, dipping at a low angle (0 to 20°) to the foliation in the host mica schists, with a thickness ranging from 0.1 to 0.5 m (Figs. 2a-3a). These veins display "en echelon" structure, being in some cases stacked onto each other (Fig. 3b). They are inter-connected by subvertical veins, dipping at a high angle (45 to 90°) to the foliation, with a thickness ranging from a few centimeters up to 0.2 m (Fig. 3c). Quartz veins dominantly strike with a NNW-SSE direction, although they have variable strikes ranging from N40°E to N170°E (Noyé 1985). The subhorizontal and subvertical veins are connected laterally with a continuous quartz filling and do not show any crosscutting relations. Although most quartz lenses taper laterally and form quartz digitations (Fig. 3d), they locally show abrupt

terminations typical of hydrofracturing. There is compelling field evidence that the vein system has been affected by ductile deformation as shown by boudinage of the subhorizontal lenticular veins showing regular mullions and asymmetric folding of the subvertical veins, with axial planes subparallel to the metamorphic foliation in the mica schists (Figs. 3e-f).

Wolframite and cassiterite formed early during emplacement of the vein system (stage I; Fig. 4) and occur as euhedral, millimetric to centimetric grains, which are dominantly found along the vein contacts with the host mica schists (Fig. 2b). Wolframite is minor relative to cassiterite and occurs as isolated crystals, sometimes forming clusters, associated with minor arsenopyrite and pyrrhotite (Fig. 5a). Cassiterite is present as clusters in the quartz veins and is associated with muscovite, albite, beryl, tourmaline, and minor F-apatite (Figs. 5b-e; 6b-c). Both wolframite and cassiterite show primary zoning, visible in optical microscopy and on μXRF maps (Figs. 6c-d; ESM Fig. 1). Wolframite has Fe-dominated compositions with structural formulae of $Fe_{0.63-0.67}Mn_{0.35-0.38}Nb_{0.01-0.02}W_{0.98-0.99}O_4$ (Harlaux et al. 2018b) whereas cassiterite is generally close to pure composition with structural formulae of $Sn_{0.95-1.00}Ti_{0.00-0.02}Fe_{0.00-0.01}Nb_{0.00-0.02}Ta_{0.00-0.01}O_2$, as determined by EMPA (ESM Table S1). Several successive hydrothermal events overprinted on the Sn-W mineralization at St-Mélany, based on field and microscopic observations (Fig. 4). These include: (i) scheelite replacing wolframite along microcracks and crystal borders, showing undulose extinction (Fig. 6e; ESM Fig. 1); (ii) chlorite ± albite veins accompanied by a polymetallic sulfide assemblage of pyrite, chalcopyrite, and minor stannite, occurring as overgrowths or vein infill within wolframite and scheelite (stage II; Figs. 5f-6f); (iii) minor quartz-adularia ± fluorite veinlets (stage III); and (iv) quartz-barite veins/breccias hosting a galena ± sphalerite mineralization (stage IV) crosscutting all previous paragenetic stages. Finally, supergene mineral phases, including anglesite, hematite, and scorodite (stage V) are observed as surficial weathering products that likely resulted from the oxidation of sulfides (mainly pyrite, arsenopyrite, and galena).

Although no crosscutting relations were observed between wolframite and cassiterite, there are several lines of evidence suggesting a temporal decoupling of W and Sn deposition: (i) wolframite and cassiterite generally do not coexist spatially and are found separately within a same vein (Figs. 5a-b). In contrast to wolframite that is restricted to the subhorizontal quartz veins, cassiterite also occurs in subvertical quartz veins and as small pods close to the vein boundaries (Fig. 5d); (ii) the ore minerals are associated with distinct mineral assemblages, i.e., arsenopyrite-pyrrhotite for wolframite and muscovite-albite-beryl-(apatite) for cassiterite. Cassiterite commonly occurs with a coarse-grained, millimeter-size muscovite fringe which is present along the vein-mica schist border (Figs. 5c-d; 6b-c), while wolframite is disseminated in quartz. Muscovite has compositions close to that of muscovite in the schists and is characterized by relative low Fe/(Fe+Mg) ratios (0.21-0.45) and F enrichment (0.2-1.0 wt.%; Noyé 1985); (iii) wolframite and cassiterite are associated with distinct textures of quartz, as shown by cross-polarized light photomicrographs and SEM-CL images (Fig. 6c-d; ESM Fig. 2). Wolframite is disseminated in large, centimeter-size quartz porphyroclasts composing in majority the mineralized veins and only shows moderate deformation characterized by undulose extinction (Fig. 6d). In contrast, cassiterite is associated with small microcrystalline quartz which formed as a result of intense ductile deformation (quartz shearing, mylonitization) and dynamic recrystallization (subgrain rotation, grain boundary migration), particularly visible along the muscovite fringe along the vein selvages (Fig. 6c). The muscovite fringe is equally deformed, showing kink-bands and micro-folds at the microscopic scale (Fig. 6b). Both cassiterite and wolframite show textural features of ductile deformation and dissolution along grain borders, and are cut by quartz veinlets showing less deformation than the main quartz composing the vein (Fig. 6d). These textural observations suggest that wolframite precipitated prior to all deformation episodes because it is associated with large, moderately-deformed

quartz zones while cassiterite formed during a later stage of deformation superimposed on the former generation of quartz.

4.2. Petrography and geochemistry of the granitic dikes

Aplitic and pegmatitic dikes crosscutting the St-Mélany vein system range from a few centimeters to 0.3 m in thickness and show variable strikes (N20-N60°) and dips (40-90°E). The granitic dikes are dominantly composed of quartz, albite, K-feldspar, and muscovite with a fine- to coarse-grained texture (Fig. 7). The dikes are deformed as evidenced by flattening perpendicular to dike orientation. Deformation is also visible at the microscopic scale, as evidenced by undulose extinction and dynamic recrystallization of quartz, bent twins in plagioclase, and kink-banded muscovite. Sericitization of feldspars is common along crystal borders and lamellar twinning. Accessory minerals disseminated in the granitic groundmass include columbite-tantalite, cassiterite, tourmaline, apatite, zircon, and uraninite. Columbite-tantalite occurs as subhedral grains ranging from 10 to 450 μm in size that are composed of successive growth zones: core (i), rims (ii-v), and overgrowth (vi; Fig. 8a-c). The rim-overgrowth interface is marked by dissolution features, indicating a multistage crystallization. In the Mn/(Fe+Mn) vs. Ta/(Ta+Nb) diagram (Fig. 8e), columbite-tantalite shows a chemical evolution from a Fe-columbite core toward a Fe-tantalite rim marked by increasing Ta/(Ta+Nb) ratios (~0.2-0.6) at near-constant Mn/(Mn+Fe) ratio (~0.2-0.4), as determined by EMPA (ESM Table S2). In contrast, the overgrowth plots into the Fe-tapiolite compositional field with Mn/(Mn+Fe) ratios close to zero and elevated Ta/(Ta+Nb) values (~0.8-0.9). Cassiterite forms subhedral grains of 100 to 450 μm in size disseminated in the granitic groundmass and locally overgrown by Fe-tapiolite (Fig. 8d). Cassiterite from the dikes ($Sn_{0.93-1.0}Ta_{0-0.04}Fe_{0-0.03}O_2$)

shows discrete zoning with rims that can reach relatively high concentrations of Ta (up to 0.04 apfu) compared to cassiterite from the quartz veins (Ta ≤ 0.01 apfu; ESM Table S1).

Whole rock geochemistry of the aplites and pegmatites is characterized by high contents of SiO_2 (72.0-75.5 wt.%) and Al_2O_3 (14.6-15.9 wt.%), moderate contents of Na_2O (2.9-4.9 wt.%), K_2O (2.3-4.1 wt.%), high content of P_2O_5 (0.4-1.1 wt.%), and low contents of Fe_2O_3 (<0.7 wt.%), MgO (<0.1 wt.%) and TiO_2 (<0.03 wt.%), and relatively high contents of CaO (0.4-1.2 wt.%) for highly fractionated granites (ESM Table S3). Aplites and pegmatites have a highly peraluminous composition (A/CNK >1.2) similar to rare metal granites and pegmatites from the FMC (Fig. 9a-b). Compared to the nearby Rocles and Borne granites (Fig. 9c-e), the aplites and pegmatites have a more evolved geochemical signature, as shown by their relatively low Fe + Mg + Ti concentrations (B parameter in Fig. 9b). Normalized trace element spectra of the aplites and pegmatites are similar (Fig. 9d) with high concentrations in incompatible elements such as Li (up to 167 ppm), Be (25-317 ppm), F (1400-3300 ppm), Rb (572-696 ppm), Cs (34-75 ppm), Ga (27-31 ppm), Nb (32-70 ppm), Ta (24-145 ppm), Sn (116-242 ppm), W (16-21 ppm), and U (4-16 ppm). The aplites and pegmatites have low REE concentrations (6-9 ppm). Their chondrite-normalized REE patterns show weak fractionation (La/Yb = 0.5-1.6) with negative Ce anomalies (Ce/Ce* = 0.5-0.9) and positive to no Eu anomalies (Eu/Eu* = 1.0-3.9; Fig. 9f).

4.3. U-Pb and $^{40}Ar/^{39}Ar$ geochronology

Coexisting centimeter-size wolframite and cassiterite from a mineralized quartz vein from St-Mélany (sample ARD-14-01) were analyzed during a single LA-ICP-MS session for U-Pb dating. The U content of wolframite is between ~3 and 26 ppm, and cassiterite is between ~5 and 140 ppm (ESM Table S4). The total Pb content is low in both minerals (0.2 to 5.8 ppm),

while the Th content is mostly <0.3 ppm. All analyses define linear trends in Tera-Wasserburg diagrams, allowing calculation of lower intercept dates, as reported below. Cassiterite analyses from the vein generally plot closer to concordia in the Tera-Wasserburg diagram than wolframite (Fig. 10a). Linear regressions through the data yield a lower-intercept date of 318.4 ± 2.2 (5.5) Ma (2σ, MSWD = 2.3) for wolframite (n = 32) with a Y-axis intercept for initial $^{207}Pb/^{206}Pb$ of 0.851 ± 0.015, and a lower-intercept date of 311.4 ± 1.0 (5.1) Ma (2σ, MSWD = 1.1) for cassiterite (n = 32) with a Y-axis intercept for initial $^{207}Pb/^{206}Pb$ of 0.876 ± 0.028 (Fig. 10a). The slightly elevated MSWD value for wolframite U-Pb data indicates that there is likely more than a single age population within the analyzed sample, however, there is not enough supporting evidence to separate them from this dataset. In contrast, the value of MSWD ≈ 1 calculated for cassiterite U-Pb data indicate a single age population at the uncertainty level of the method. Six out of 38 data points were excluded from the cassiterite dataset and represent outliers in their U-Pb composition which are not representative of the main population. The wolframite LA-ICP-MS U-Pb age falls within uncertainty of the previous wolframite ID-TIMS U-Pb age of 315 ± 15 Ma (2σ) obtained on the same sample (Harlaux et al. 2018a). Cassiterite from granitic pegmatite dikes (samples ARD-13-22 and ARD-13-72) crosscutting the St-Mélany vein system was analyzed during a separate LA-ICP-MS session. The cassiterite grains are ca. 100-200 µm in size and show primary growth zoning as revealed by SEM-CL images (ESM Fig. 3). The U and Pb contents of cassiterite are low, between 1.5 and 19 ppm and 0.1 and 3.6 ppm, respectively (Table S4). Linear regression through the data yields a lower-intercept date of 305.9 ± 3.9 (6.3) Ma (2σ, MSWD = 2.1) for pegmatite cassiterite (n = 48) with a Y-axis intercept for initial $^{207}Pb/^{206}Pb$ of 0.842 ± 0.001 (Fig. 10b).

In situ $^{40}Ar/^{39}Ar$ analyses were done on coarse-grained muscovite from the selvage of a mineralized quartz vein (sample ARD-13-12). Muscovite was studied by optical microscopy and SEM prior to $^{40}Ar/^{39}Ar$ dating to characterize mineral textures and to identify any chemical

zoning and micro-inclusions. At the microscopic scale, muscovite is relatively homogeneous optically, but exhibits chemical zoning on BSE images and secondary dissolution-precipitation features along grain borders and micro-fractures with minor chlorite infill along interstitial planes (ESM Fig. 4). The in situ laser spots were positioned in the least altered domains of muscovite, and the $^{40}Ar/^{39}Ar$ isotopic analyses yield highly radiogenic compositions, with $^{40}Ar^*$ content ranging between 96.8 and 100% (ESM Table S5). The calculated apparent ages range from 294.0 ± 5.5 to 319.6 ± 8.5 Ma (n = 8) and yield a weighted mean date of 304.5 ± 4.8 Ma (2σ, MSWD = 2.2; Fig. 11).

5. Discussion

5.1. Timing of magmatic/hydrothermal events within the regional polyphase tectono-metamorphic setting

Field observations at St-Mélany show that the mineralized veins crosscut both the metamorphic foliation and the syn-foliation quartz lenses in the mica schists and were emplaced by hydrofracturing of the host rocks. Syn-foliation quartz lenses are widespread in the Cévennes Schist Formation and were formed along shear zones under Barrovian metamorphic conditions (500°C, 450 MPa) during crustal thickening and nappe stacking related to the D2 compressive event (ca. 340-330 Ma; Arnaud et al. 2004). The mineralized quartz veins at St-Mélany, both at the macroscopic and microscopic scales, show evidence of ductile deformation (boudinage, asymmetric folding) and dynamic recrystallization (subgrain rotation, grain boundary migration) at high temperature (T >450°C; Stipp et al. 2002). The subhorizontal and subvertical veins are connected laterally and show a continuous internal structure and quartz filling without crosscutting relations, indicating simultaneous opening under conditions of hydraulic

498 overpressures, as described in other peri-granitic W-Sn vein-type deposits (Jacques et al. 2018).
499 Cassiterite and wolframite are also affected by ductile deformation, as shown by our
500 microstructural observations, and precipitated at temperatures of ca. 350-400°C, as reported by
501 previous fluid inclusion work (Noyé 1985). These lines of evidence demonstrate that the St-
502 Mélany vein system was emplaced after the major D2 event (ca. 340-330 Ma) and during the
503 D3 event (ca. 325-315 Ma; Barbey et al. 2015), i.e., contemporaneous with the regional low
504 pressure – moderate temperature metamorphism.
505 The LA-ICP-MS U-Pb dates of 318.4 ± 2.2 (5.5) Ma for wolframite and 311.4 ± 1.0 (5.1) Ma
506 for cassiterite, both interpreted as crystallization ages, support an emplacement age of the
507 mineralized veins during the D3 event. Considering that these two minerals were analyzed
508 within the same thin section and during the same analytical section with identical acquisition
509 parameters, we can exclude the external error quantifying the long-term reproducibility
510 (Horstwood et al. 2016). Thus, it appears from these data that wolframite and cassiterite were
511 deposited with a time gap of 4 to 10 Myr. However, it must be emphasized that these data were
512 obtained on a single thin section and that only two grains of wolframite and cassiterite were
513 analyzed. Additionally, the cassiterite-bearing veins are highly deformed which may potentially
514 cause a disturbance of the U-Pb isotope system of cassiterite resulting in partial age resetting.
515 Therefore, we consider that more work is needed to investigate the existence of multiple W-Sn
516 mineralization events in the study area with additional geochronological data.
517 The younger $^{40}Ar/^{39}Ar$ date of 304.5 ± 4.8 Ma obtained on muscovite from a vein selvage can
518 be interpreted either as a recrystallization age or as a cooling age caused by partial resetting of
519 the Ar isotopic system. Deformation of the quartz veins may have affected the chemistry of the
520 micas along recrystallized domains which will lead to a rejuvenation of the $^{40}Ar/^{39}Ar$ date
521 (provided it is not affected by excess Ar). Previous work from Noyé (1985) indicates that
522 muscovite compositions are relatively homogeneous at the grain scale and do not reveal

chemically-distinct domains. This is not supported by our observations which show intra-grain chemical zoning and alteration features on BSE images (ESM Fig. 4). Considering that muscovite is deformed and shows chemical zoning at the microscopic scale, we interpret the obtained $^{40}Ar/^{39}Ar$ date as a recrystallization age resulting from metamorphic re-equilibration or hydrothermal overprint.

The mineralized veins at St-Mélany are cut by northeast-striking granitic dikes, showing an apparent normal displacement (Fig. 2c). The LA-ICP-MS U-Pb date of 305.9 ± 3.9 (6.3) Ma on magmatic cassiterite is interpreted as a crystallization age and is consistent with the previously obtained $^{40}Ar/^{39}Ar$ muscovite plateau age of 306.5 ± 3.1 Ma (Chauvet et al. 2012). This indicates that the granitic dikes were emplaced during regional northwest-southeast extension at the D3-D4 transition (ca. 310-300 Ma; ESM Fig. 5). Lamprophyre dikes crosscutting the vein system have not been dated but they were likely emplaced during the extensional D4 event (ca. 305 Ma) coevally with other lamprophyre dikes located south of St-Mélany and vaugnerite bodies in the southern border of the Velay anatectic dome (Couzinié et al. 2014; Barbey et al. 2015; Laurent et al. 2017). A schematic diagram summarizing the polyphase evolution of the St-Mélany vein system is shown in Figure 12.

5.2. Role of the granitic plutons as source of the mineralizing fluids at St-Mélany

The close spatial relationships between the St-Mélany occurrence and the nearby Borne and Rocles granites raises the question of their role as proximal sources for the mineralizing fluids. The metaluminous to peraluminous Borne granite has relatively high concentrations in Fe, Mg and Ti, and overlaps in compositions with the more felsic members of vaugnerites from the southern FMC (Fig. 9). Its poorly evolved geochemical signature and its younger emplacement age (309.7 ± 3.6 Ma to 302.5 ± 0.9 Ma; Brichau et al. 2008; Couzinié 2017; Laurent et al. 2017)

548 relative to the wolframite and cassiterite veins, preclude its role as a source of mineralizing
549 fluids at St-Mélany. In contrast, the Rocles granite is characterized by a more evolved
550 peraluminous felsic composition (Fig. 9) and was emplaced during the D3 event according to
551 existing geochronological data (325 ± 4 to 318 ± 3 Ma; Be Mezeme et al. 2006, 2007; Couzinié
552 2017). The muscovite-rich Rocles granite, located less than 2 km of St-Mélany, is the most
553 evolved unit of the Rocles pluton as indicated by relatively high concentrations of Sn (46 ppm),
554 W (6 ppm), Be (39 ppm), Nb (20 ppm), Ta (18 ppm), and low Nb/Ta ratio ~1.1 (ESM Table
555 S3), which is characteristic of Sn-W-related granites (Ballouard et al. 2016). In contrast, the
556 Borne granite and other units from the Rocles pluton are relatively depleted in those elements
557 and have high Nb/Ta ratios >7, supporting a low metallogenic potential. Therefore, we propose
558 that the muscovite-rich Rocles granite emplaced at 319.8 ± 3.8 Ma (U-Pb zircon; Couzinié
559 2017) is a potential source for W-rich magmatic fluids forming the St-Mélany mineralization
560 at ca. 318 Ma.
561 Previous fluid inclusion work suggested that the mineralized quartz veins at St-Mélany resulted
562 from the mixing of aqueous-carbonic fluids (CO_2-CH_4±N_2-rich) of moderate temperature (350-
563 450°C) and moderate salinity (5-8 wt.% NaCl eq) with aqueous fluids of lower temperature
564 (120-200°C) and lower salinity (1-3 wt.% NaCl eq), possibly of meteoric origin (Noyé 1985).
565 The early C-O-H-N fluids are typical of peribatholitic W(-Sn) deposits in the FMC and are
566 interpreted either as metamorphic fluids equilibrated at high-temperature with graphite-bearing
567 metasedimentary rocks or as magmatic fluids that interacted with the metamorphic basement
568 (Ramboz et al. 1985; Cuney et al. 1992; Vallance et al. 2001; Lerouge and Bouchot 2009;
569 Harlaux et al. 2021). High-temperature fluid-rock interactions were likely responsible for W
570 deposition at St-Mélany, as indicated by the Fe-rich composition of wolframite (Harlaux et al.
571 2018b; Michaud and Pichavant 2019). Considering the synchronicity of granitic magmatism
572 and regional metamorphism in the North Cévennes area during the 320-300 Ma period, it is

possible that both magmatic and metamorphic fluids were involved in the formation of the St-Mélany vein system. The large thermal anomaly induced by the emplacement of granitic bodies in the area may have generated contact metamorphic fluids by dehydration of the host mica schists, or may have driven advective flow of earlier regional metamorphic fluids, as proposed for the Panasqueira W(-Sn) deposit in Portugal (Cathelineau et al. 2020; Carocci et al. 2021). Such large-scale hydrothermal circulations may have leached W from the regional granites, gneisses, and mica schists, which can contain significant amounts of W-rich minerals (100s-1000s ppm) such as micas and Ti-oxides (Harlaux 2016; El Korh et al. 2020; Harlaux et al. 2021; Monnier et al. 2022).

Based on available geochemical and geochronological data, we favor the muscovite-rich Rocles granite as a proximal source of W-mineralizing fluids at St-Mélany, but we cannot rule out the involvement of metamorphic fluids. This magmatic-metamorphic evolution ended with the formation of shear zone-hosted orogenic gold mineralization in the southern Cévennes area during the regional D4 extension at ca. 305-300 Ma (Bouchot et al. 2005; Chauvet et al. 2012).

5.3. Characteristics and origin of the granitic dikes from St-Mélany

The dikes of aplites and pegmatites at St-Mélany have highly fractionated peraluminous compositions and host disseminated magmatic mineralization of cassiterite and columbite-tantalite. Aplite-pegmatite dikes show a depletion in Fe, Mg, and Ti and in elements typically compatible in peraluminous magmas such as Zr, Th, and REE (Fig. 9). The dikes have high concentrations in P and incompatible elements, including Li, Be, F, Rb, Cs, U, Nb, Ta, Sn, and W, along with low Nb/Ta (0.5-1.5) ratios. Such highly evolved compositions contrast with the nearby Rocles and Borne granites. The mineralogical and geochemical features of the St-Mélany aplites-pegmatites are characteristic of peraluminous high-phosphorus rare metal

598 granites (PHP-RMG) as defined by Linnen and Cuney (2005). Compared to the Beauvoir RMG
599 in the northwestern FMC (Cuney et al. 1992; Raimbault et al. 1995), the granitic dikes from St-
600 Mélany are less evolved and could represent peraluminous RMG magmas "en route" to the
601 surface, as discussed by Marignac et al. (2009) and Tartèse and Boulvais (2010).
602 The trend of increasing Ta/(Ta+Nb) ratio at near-constant Mn/(Mn+Fe) ratio from core to rim
603 in columbite-tantalite, characteristic of LCT pegmatites, is interpreted as reflecting progressive
604 magmatic fractionation of the peraluminous silicate melt due to the higher solubility of tantalite
605 relative to columbite (Linnen and Keppler 1997; Linnen and Cuney 2005; Breiter et al. 2007;
606 Van Lichtervelde et al. 2007). In contrast, late Fe-tapiolite overgrowths on magmatic cassiterite
607 and columbite-tantalite could result of disequilibrium crystallization or fluid-mineral
608 interaction during the magmatic-hydrothermal transition (Zhu et al. 2015; Wu et al. 2018; Van
609 Lichtervelde et al. 2018; Michaud and Pichavant 2020; Ballouard et al. 2020).
610 The emplacement age of granitic dikes from St-Mélany (306.5 ± 3.1 Ma to 305.9 ± 3.9 Ma)
611 overlap with the age period of ca. 310-315 Ma for RMG magmatism in the northwestern FMC
612 (Cuney et al. 2002; Cuney and Barbey 2014; Melleton et al. 2015; Harlaux et al. 2021; Marcoux
613 et al. 2021) and represent a new occurrence of PHP-RMG in the southern FMC. Due to their
614 distinct chemistry and age relative to the granites of Rocles (ca. 325-315 Ma) and Borne (ca.
615 310-305 Ma), the aplitic and pegmatitic dikes from St-Mélany might be genetically related to
616 a concealed RMG intrusion. While cassiterite in the quartz veins was mostly unaffected by
617 hydrothermal overprint, as shown by primary zoning and minor dissolution features on the
618 µXRF element maps (ESM Fig. 1), wolframite was partially replaced by scheelite (Fig. 6e).
619 This process may result from a change of fluid composition (e.g., Ca/Fe ratio) or pressure
620 decrease (Wood and Samson 2000; Liu et al. 2021) related to the late-orogenic exhumation that
621 occurred during the D3-D4 transition. Considering the long term reproducibility of the U-Pb
622 ages for magmatic cassiterite (305.9 ± 3.9 (6.3) Ma) and hydrothermal cassiterite (311.4 ± 1.0

623 (5.1) Ma), analyzed during separate LA-ICP-MS analytical sessions, we can define an overlap
624 around 312-306 Ma, which coincides with emplacement of the Pont-de-Montvert-Borne
625 granitic pluton. Thus, it is possible that Sn-rich magmatic fluids exsolved from the granitic
626 dikes overprinted the W-mineralized vein system, resulting in the precipitation of hydrothermal
627 cassiterite and associated minerals (albite, muscovite, beryl, F-apatite) along the vein-mica
628 schist borders.
629
630 *5.4. Implications for crustal melting conditions in the southeastern FMC*
631
632 The St-Mélany occurrence represents a new evidence of peribatholitic W(-Sn) hydrothermal
633 mineralization overprinted by RMG magmatism in the European Variscan belt. Similar
634 relationships have been reported in the northwestern FMC at Echassières (Cuney et al. 1992;
635 Harlaux et al. 2017; Monnier et al. 2019, 2020) and Puy-les-Vignes (Harlaux et al. 2021), as
636 well as in the Iberian Massif at Panasqueira (Marignac et al. 2020). This spatial superimposition
637 can be interpreted as a marker of major changes in crustal melting conditions in this part of the
638 FMC during the late Carboniferous. The Sn-W mineralization at St-Mélany was formed during
639 the 320-310 Ma period which is contemporaneous with the regional low pressure – medium
640 temperature M3 metamorphism (ESM Fig. 5; Barbey et al. 2015). This dominantly water-
641 fluxed melting event reaching muscovite-breakdown conditions (T <750°C, P = 0.5-0.7 GPa;
642 Barbey et al. 2015) resulted in the formation of MPG magmas and emplacement of the Rocles
643 pluton.
644 Following the M3 event, the granitic dikes of St-Mélany were emplaced at ca. 305 Ma coevally
645 with the regional low pressure – high temperature M4 metamorphism reaching biotite
646 dehydration-melting conditions (T >800°C, P = 0.3-0.4 GPa; Barbey et al. 2015; Villaros et al.
647 2018; ESM Fig. 5). This high-temperature event led to the formation of the Velay anatectic

dome and is possibly linked to lower crust granulitization (Pin and Vielzeuf 1983; Costa et al. 1993). Recent experimental petrology studies showed that mica dehydration-melting in fluid-absent conditions can produce MPG as commonly encountered in the FMC but fail to reproduce RMG compositions (Michaud et al. 2021). Accordingly, the formation of RMG magmas could be explained by two possible, not mutually exclusive scenarios, i.e., (i) water-fluxed melting, and (ii) residual source/restite melting (Michaud et al. 2021).

Granulite-facies metamorphism of the lower continental crust induced by carbonic fluid waves during delamination of the subcontinental lithospheric mantle can liberate large amounts of biotite-hosted fluxing elements (i.e., F, Li, P, B) and rare metals (i.e., Sn, W, Nb, Ta, Cs); partial melting of the intermediate crust in the presence of such fluids has been proposed as a mechanism for the generation of RMG melts in the FMC (Cuney and Barbey 2014). This model accounts for many geological features in the FMC and may also explain the formation of RMG and lamprophyres dikes at St-Mélany in response to a major crustal thermal anomaly. An alternative model may be successive melting events with multiple melt extraction, potentially producing RMG magmas at high temperature (Wolf et al. 2018; Michaud et al. 2021). In this second model, muscovite dehydration-melting conditions are attained first, producing MPG melts and Nb-Ta-rich restites, followed secondly by biotite dehydration-melting at higher temperature of restitic lithologies and the generation of peraluminous RMG melts. Therefore, the polyphase emplacement at St-Mélany of Sn-W-mineralized veins at ca. 320-310 Ma and rare metal granitic dikes at ca. 305 Ma reflects contrasting crustal melting conditions in relation to the late Carboniferous orogenic evolution of the southeastern FMC, possibly related to delamination of the subcontinental lithospheric mantle.

6. Conclusions

673 The St-Mélany Sn-W vein system records multiple magmatic-hydrothermal events within a
674 regional polyphase tectono-metamorphic setting. The mineralized quartz veins show evidence
675 of ductile deformation (boudinage, asymmetric folding, dynamic recrystallization) consistent
676 with a synkinematic emplacement during the regional low pressure – medium temperature
677 metamorphism at ca. 320-315 Ma. This event was synchronous with the emplacement of the
678 syntectonic Rocles peraluminous granite, which represents a possible proximal source for the
679 mineralizing fluids. The U-Pb LA-ICP-MS ages for coexisting wolframite (318.4 ± 2.2 Ma)
680 and cassiterite (311.4 ± 1.0 Ma) in quartz veins suggest a temporal decoupling of W and Sn
681 mineralization, but additional work is needed to confirm this interpretation. Dikes of aplites and
682 pegmatites cut the mineralized veins and were emplaced at 305.9 ± 3.9 Ma based on U-Pb LA-
683 ICP-MS cassiterite dating. The dikes have highly evolved compositions typical of peraluminous
684 high-phosphorus rare metal granites with Li-F-Ta>Nb-Sn-Be enrichments. We conclude that
685 polyphase emplacement of W-Sn-mineralized veins at ca. 320-310 Ma and rare metal granitic
686 dikes at ca. 305 Ma results from contrasting crustal melting conditions, in relation to the late
687 Carboniferous orogenic evolution of the southeastern FMC, possibly related to delamination of
688 the subcontinental lithospheric mantle.
689
690 **Acknowledgments**
691
692 This research was supported by the French National Research Agency through the national
693 program “Investissements d’avenir” of the Labex Ressources 21 (ANR-10-LABX-21-
694 RESSOURCES21) and the ERAMIN project NewOres (ANR-14-EMIN-0001). The authors
695 are grateful to Andreï Lecomte, Olivier Rouer, Chantal Peiffert, and Emeline Moreira
696 (GeoRessources, France) for their technical assistance during the acquisition of SEM, EMPA,
697 and LA-ICP-MS data. Simon Couzinié is thanked for stimulating discussions. Finally, we

would like to thank the Associate Editor Fernando Tornos, the Editor-in-Chief Bernd Lehmann, as well as Rolf Romer and two anonymous reviewers, for their insightful comments and suggestions, which helped to improve the original manuscript.

Conflict of interest

The authors declare that they have no known competing financial interest or personal relationship that could have appeared to influence the work reported in this article.

705 **References**

706

707 Angel JM, Bertrand G (2018) PotTer – Evaluation du potentiel en terre en antimoine et
708 tungstène de la France métropolitaine. Rapport Public BRGM/RP-67478-FR, 116p.

709 Aquilina L, Boulvais P, Mossmann JR (2011) Fluid migration at the basement/sediment
710 interface along the margin of the Southeast basin (France): implications for Pb–Zn ore
711 formation. Miner Deposita 46:959-979.

712 Aït-Malek H (1997) Pétrologie, géochimie et géochronologie d'associations acides-basiques:
713 exemples du Sud-Est du Velay (Massif Central Français) et de l'Anti-Atlas occidental
714 (Maroc). Unpublished Ph.D. thesis, Institut National Polytechnique de Lorraine, Nancy,
715 268p.

716 Arnaud F, Boullier AM, Burg JP (2004) Shear structures and microstructures in micaschists:
717 the Variscan Cévennes duplex (French Massif Central). J Struct Geol 26:855-868.

718 Aubert G (1969) Les coupoles granitiques de Montebras et d'Echassières (Massif Central
719 Français) et la genèse de leurs minéralisations en étain, lithium, tungstène et béryllium.
720 Mem BRGM 46:350.

721 Ballouard C, Poujol M, Boulvais P, Branquet Y, Tartèse R, Vigneresse JL (2016) Nb-Ta
722 fractionation in peraluminous granites: A marker of the magmatic-hydrothermal
723 transition. Geology 44:231-234.

724 Ballouard C, Elburg MA, Tappe S, Reinke C, Ueckermann H, Doggart S (2020) Magmatic-
725 hydrothermal evolution of rare metal pegmatites from the Mesoproterozoic Orange River
726 pegmatite belt (Namaqualand, South Africa). Ore Geol Rev 116:103252.

727 Barbarin B (1999) A review of the relationships between granitoid types, their origins and their
728 geodynamic environments. Lithos 46:605–626.

729 Barbey P, Villaros A, Marignac C, Montel JM (2015) Multiphase melting, magma
730 emplacement and P-T-time path in late-collisional context: the Velay example (Massif
731 Central, France). B Soc Geol Fr 186:93-116.
732 Be Mezeme E, Cocherie A, Faure M, Legendre O, Rossi P (2006) Electron microprobe
733 monazite geochronology of magmatic events: examples from Variscan migmatites and
734 granitoids, Massif Central, France. Lithos 87:276-288.
735 Be Mezeme E, Faure M, Chen Y, Cocherie A, Talbot JY (2007) Structural, AMS and
736 geochronological study of a laccolith emplaced during Late Variscan orogenic extension:
737 the Rocles pluton (SE French Massif Central). Int J Earth Sci 96:215-228.
738 Bellanger D (1980) Vaugnérites et roches associées des Cévennes médianes : Quelques aspects
739 pétrologiques et géochimiques. Unpublished Ph.D. thesis, Université de Lyon, France,
740 185p.
741 Béziat P, Prouhet JP, Tollon F (1980) Le district de Montredon-Labessonnié (Tarn): W, Sn, F.
742 26e Cong Geol Intern Paris: Gisements français 7, 42 p.
743 Bouchot V, Ledru P, Lerouge C, Lescuyer JL, Milesi JP (2005) Late Variscan mineralizing
744 systems related to orogenic processes: The French Massif Central. Ore Geol Rev 27:169-
745 197.
746 Bouilhol P, Leyreloup AF, Delor C, Vauchez A, Monié P (2006) Relationships between lower
747 and upper crust tectonic during doming: the mylonitic southern edge of the Velay
748 metamorphic core complex (Cévennes-French Massif Central). Geodin Acta 19:137-153.
749 Breiter K, Škoda R, Uher P (2007) Nb–Ta–Ti–W–Sn–oxide minerals as indicators of a
750 peraluminous P-and F-rich granitic system evolution: Podlesí, Czech Republic. Miner
751 Petrol 91:225–248.
752 Breiter K, Ďurišová J, Hrstka T, Korbelová Z, Vaňková MH, Galiová MV, Kanický V,
753 Rambousek P, Knésl I, Dobeš P, Dosbaba M (2017) Assessment of magmatic vs.

754 metasomatic processes in rare-metal granites: a case study of the Cínovec/Zinnwald Sn–
755 W–Li deposit, Central Europe. Lithos 292:198-217.
756 Brichau S, Respaut JP, Monié P (2008) New age constraints on emplacement of the Cévenol
757 granitoids, South French Massif Central. Int J Earth Sci 97:725-738.
758 Carignan J, Hild P, Mevelle G, Morel J, Yeghicheyan D (2001) Routine analyses of trace
759 elements in geological samples using flow injection and low pressure online liquid
760 chromatography coupled to ICP-MS: A study of geochemical reference materials BR, DR-
761 N, UB-N, AN-G and GH. Geostand Newslett 25:187-198.
762 Carocci E, Marignac C, Cathelineau M, Truche L, Poujol M, Boiron MC, Pinto F (2021)
763 Incipient Wolframite deposition at Panasqueira (Portugal): W-Rich rutile and tourmaline
764 compositions as proxies for the early fluid composition. Econ Geol 116:123-146.
765 Carr PA, Zink S, Bennett VC, Norman MD, Amelin Y, Blevin PL (2020) A new method for U-
766 Pb geochronology of cassiterite by ID-TIMS applied to the Mole Granite polymetallic
767 system, eastern Australia. Chem Geol 539:119539.
768 Carr PA, Mercadier J, Harlaux M, Romer RL, Moreira E, Legros H, Cuney M, Marignac M,
769 Cauzid J, Salsi L, Lecomte A, Rouer O, Peiffert C (2021) U/Pb geochronology of
770 wolframite by LA-ICP-MS; mineralogical constraints, analytical procedures, data
771 interpretation, and comparison with ID-TIMS. Chem Geol 584:120511.
772 Carr PA, Moreira E, Neymark L, Norman MD, Mercadier J (2022) A LA-ICP-MS Comparison
773 of Reference Materials Used in Cassiterite U-Pb Geochronology. Geostand Geoanal Res
774 47:67-87.
775 Cathelineau M, Boiron MC, Marignac C, Dour M, Dejean M, Carocci E, Truche L, Pinto F
776 (2020) High pressure and temperatures during the early stages of tungsten deposition at
777 Panasqueira revealed by fluid inclusions in topaz. Ore Geol Rev 126:103741.

778 Černý P, Blevin PL, Cuney M, London D (2005) Granite-related ore deposits. Econ Geol
779 100:337–370.
780 Chauvet A, Volland-Tuduri N, Lerouge C, Bouchot V, Monié P, Charonnat X, Faure M (2012)
781 Geochronological and geochemical characterization of magmatic-hydrothermal events
782 within the Southern Variscan external domain (Cévennes area, France). Int J Earth Sci
783 101:69-86.
784 Chelle-Michou C, Laurent O, Moyen JF, Block S, Paquette JL, Couzinié S, Gardien V,
785 Vanderhaeghe O, Villaros A, Zeh A (2017) Pre-Cadomian to late-Variscan odyssey of the
786 eastern Massif Central, France: formation of the West European crust in a nutshell.
787 Gondwana Res 46:170–190.
788 Chew DM, Petrus JA, Kamber BS (2014) U–Pb LA–ICPMS dating using accessory mineral
789 standards with variable common Pb. Chem Geol 363:185-199.
790 Costa S, Rey P, Todt W (1993) Late Carboniferous age of lower-crustal granulite facies
791 xenoliths in the eastern French Massif Central: implications for post-thickening crustal
792 processes. Terra Nova 5:233.
793 Couzinié S (2017) Evolution of the continental crust and significance of the zircon record, a
794 case study from the French Massif Central. Unpublished Ph.D. thesis, Université de Lyon
795 and Université Jean Monnet, Saint-Etienne, France, 431p.
796 Couzinié S, Moyen JF, Villaros A, Paquette JL, Scarrow JH, Marignac C (2014) Temporal
797 relationships between Mg-K mafic magmatism and catastrophic melting of the Variscan
798 crust in the southern part of Velay complex (Massif Central, France). J Geosci 59:69-86.
799 Couzinié S, Laurent O, Poujol M, Mintrone M, Chelle-Michou C, Moyen JF, Bouilhol P,
800 Vezinet A, Marko L (2017) Cadomian S-type granites as basement rocks of the Variscan
801 belt (Massif Central, France): Implications for the crustal evolution of the north Gondwana
802 margin. Lithos 286:16-34.

803 Couzinié S, Laurent O, Chelle-Michou C, Bouilhol P, Paquette JL, Gannoun AM, Moyen JF
804 (2019) Detrital zircon U–Pb–Hf systematics of Ediacaran metasediments from the French
805 Massif Central: Consequences for the crustal evolution of the north Gondwana margin.
806 Precambrian Res 324:269-284.
807 Couzinié S, Bouilhol P, Laurent O, Grocolas T, Montel JM (2022) Cambro–Ordovician
808 ferrosilicic magmatism along the northern Gondwana margin: constraints from the
809 Cézarenque–Joyeuse gneiss complex (French Massif Central). BSGF - Earth Sci Bull
810 193:15.
811 Cuney M, Barbey P (2014) Uranium, rare metals, and granulite-facies metamorphism. Geosci
812 Front 5:729-745.
813 Cuney M, Marignac C, Weisbrod A (1992) The Beauvoir topaz-lepidolite albite granite (Massif
814 Central, France): The disseminated magmatic Sn-Li-Ta-Nb-Be mineralization. Econ Geol
815 87:1766-1794.
816 Cuney M, Alexandrov P, Le Carlier de Veslud C, Cheilletz A, Raimbault L, Ruffet G, Scaillet
817 S (2002) The timing of W-Sn-rare metals mineral deposit formation in the Western
818 Variscan chain in their orogenic setting: the case of the Limousin area (Massif Central,
819 France). Geol Soc London Spec Publ 204:213–228.
820 Debon F, Le Fort P (1983) A chemical-mineralogical classification of common plutonic rocks
821 and associations. Trans R Soc Edinb 73:135–149.
822 Deino AL (2013) Berkeley Geochronology Center, Mass Spec, $^{40}Ar/^{39}Ar$ data measurement
823 and reduction software. http://www.bgc.org/facilities/other_facil.html.
824 Didier A, Bosse V, Boulvais P, Bouloton J, Paquette JL, Montel JM, Devidal JL (2013)
825 Disturbance versus preservation of U–Th–Pb ages in monazite during fluid–rock
826 interaction: textural, chemical and isotopic in situ study in microgranites (Velay Dome,
827 France). Contrib Mineral Petr 165:1051-1072.

El Korh A, Boiron MC, Cathelineau M, Deloule E, Luais B (2020) Tracing metallic pre-concentrations in the Limousin ophiolite-derived rocks and Variscan granites (French Massif Central). Lithos 356:105345.

Faure M, Charonnat X, Chauvet A (1999) Schéma structural et évolution tectonique du domaine para-autochtone cévenol de la chaîne hercynienne (Massif central français). CR Acad Sci 328:401-407.

Faure M, Charonnat X, Chauvet A, Chen Y, Talbot JY, Martelet G, Courrioux G, Monié P, Milesi JP (2001) Tectonic evolution of the Cévennes para-autochthonous domain of the Hercynian French Massif Central and its bearing on ore deposits formation. B Soc Geol Fr 172:687-696.

Faure M, Lardeaux JM, Ledru P (2009) A review of the pre-Permian geology of the Variscan French Massif Central. CR Geosci 341:202–213.

González TL, Polonio FG, Moro FJL, Fernández AF, Contreras JLS, Benito MCM (2017) Tin-tantalum-niobium mineralization in the Penouta deposit (NW Spain): Textural features and mineral chemistry to unravel the genesis and evolution of cassiterite and columbite group minerals in a peraluminous system. Ore Geol Rev 81:79-95.

Gourcerol B, Gloaguen E, Melleton J, Tuduri J, Galiegue X (2019) Re-assessing the European lithium resource potential–A review of hard-rock resources and metallogeny. Ore Geol Rev 109:494-519.

Gourcerol B, Gutierrez T, Pochon A, Picault M, Gloaguen E, Fournier E (2021) Evolution Base de données “Gisements France”: Atlas des substances critiques et stratégiques. Rapport Public BRGM/RP-71133-FR, 66p.

Guion JL, Béziat P, Tollon F (1985) Données nouvelles sur les paragenèses du champ filonien à wolframite de Lacoste, district de Montredon-Labessonnié (Tarn). B Mineral 108:391-402.

853 Harlaux M (2016) Tungsten and rare-metal (Nb, Ta, Sn) hydrothermal metallogenic systems in
854 the late-Variscan orogenic context: Example of the French Massif Central. Unpublished
855 Ph.D. thesis, Université de Lorraine, Nancy, France, 576 p.
856 Harlaux M, Mercadier J, Bonzi WME, Kremer V, Marignac C, Cuney M (2017) Geochemical
857 signature of magmatic-hydrothermal fluids exsolved from the Beauvoir rare-metal granite
858 (Massif Central, France): insights from LA-ICPMS analysis of primary fluid inclusions.
859 Geofluids 2017:1–25.
860 Harlaux M, Romer RL, Mercadier J, Morlot C, Marignac C, Cuney M (2018a) 40 Ma of
861 hydrothermal W mineralization during the Variscan orogenic evolution of the French
862 Massif Central revealed by U-Pb dating of wolframite. Miner Deposita 53:21-51.
863 Harlaux M, Mercadier J, Marignac C, Peiffert C, Cloquet C, Cuney M (2018b) Tracing metal
864 sources in peribatholitic hydrothermal W deposits based on the chemical composition of
865 wolframite: The example of the Variscan French Massif Central. Chem Geol 479:58-85.
866 Harlaux M, Mercadier J, Marignac C, Villeneuve J, Mouthier B, Cuney M (2019) Origin of the
867 atypical Puy-les-Vignes W breccia pipe (Massif Central, France) constrained by trace
868 element and boron isotopic composition of tourmaline. Ore Geol Rev 114:103132.
869 Harlaux M, Marignac C, Mercadier J, Poujol M, Boiron MC, Kouzmanov K, Camacho A,
870 Alikouss S, Roméo B, Mouthier B, Cuney M (2021) Multistage development of a
871 hydrothermal W deposit during the Variscan late-orogenic evolution: The Puy-les-Vignes
872 breccia pipe (Massif Central, France). BSGF - Earth Sci Bull 192:33.
873 Horstwood MS, Košler J, Gehrels G, Jackson SE, McLean NM, Paton C, Pearson NJ, Sircombe
874 K, Sylvester P, Vermeesch P, Bowring JF (2016) Community-derived standards for LA-
875 ICP-MS U-(Th-)-Pb geochronology - Uncertainty propagation, age interpretation and data
876 reporting. Geostand Geoanal Res 40:311-332.

877 Jacques D, Vieira R, Muchez P, Sintubin M (2018) Transpressional folding and associated
878 cross-fold jointing controlling the geometry of post-orogenic vein-type W-Sn
879 mineralization: examples from Minas da Panasqueira, Portugal. Miner Deposita 53:171-
880 194.
881 Jochum KP, Stoll B (2008) Reference materials for elemental and isotopic analyses by LA-
882 (MC)-ICP-MS: Successes and outstanding needs. Mineralogical Association of Canada
883 Short Course 40:147-168.
884 Kuiper KF, Deino A, Hilgen FJ, Krijgsman W, Renne R, Wijbrans JR (2008) Synchronizing
885 Rock Clocks of Earth History. Science 320:500-504.
886 Laurent O, Couzinié S, Zeh A, Vanderhaeghe O, Moyen JF, Villaros A, Gardien V, Chelle-
887 Michou C (2017) Protracted, coeval crust and mantle melting during Variscan late-
888 orogenic evolution: U–Pb dating in the eastern French Massif Central. Int J Earth Sci
889 106:421-451.
890 Ledru P, Courrioux G, Dallain C, Lardeaux JM, Montel JM, Vanderhaeghe O, Vitel G (2001)
891 The Velay dome (French Massif Central): melt generation and granite emplacement during
892 orogenic evolution. Tectonophysics 342:207-237.
893 Legros H, Harlaux M, Mercadier J, Romer RL, Poujol M, Camacho A, Marignac C, Cuney M,
894 Wang RC, Charles N, Lespinasse MY (2020) The world-class Nanling metallogenic belt
895 (Jiangxi, China): W and Sn deposition at 160 Ma followed by 30 m.y. of hydrothermal
896 metal redistribution. Ore Geol Rev 117:103302.
897 Lehmann B (2021) Formation of tin ore deposits: A reassessment. Lithos 402:105756.
898 Lerouge C, Bouchot V (2009) Conditions of formation and origin of fluids of quartz-tourmaline
899 veins in the La Châtaigneraie tungstiferous district (Massif Central, France): fluid
900 inclusions and stable isotopes. B Soc Geol Fr 180:263-270.

Lerouge C, Deschamps Y, Piantone P, Gilles C, Breton J (2007) Metal-carrier accessory minerals associated with W±Sn mineralization, La Châtaigneraie tungsten ore district, Massif Central, France. Can Mineral 45:875-889.

Linnen RL, Keppler H (1997) Columbite solubility in granitic melts: consequences for the enrichment and fractionation of Nb and Ta in the Earth's crust. Contrib Mineral Petr 128:213-227.

Linnen RL, Cuney M (2005) Granite-related rare-element deposits and experimental constraints on Ta-Nb-W-Sn-Zr-Hf mineralization. In Rare-Element Geochemistry and Mineral Deposits (eds. RL Linnen and IM Samson). Geol Assoc Canada Short Course Notes 17:45-68.

Liu X, Xiao C, Wang Y (2021) The relative solubilities of wolframite and scheelite in hydrothermal fluids: Insights from thermodynamic modeling. Chem Geol 584:120488.

Lotout C, Pitra P, Poujol M, Anczkiewicz R, Van Den Driessche J (2018) Timing and duration of Variscan high-pressure metamorphism in the French Massif Central: A multimethod geochronological study from the Najac Massif. Lithos 308:381–394.

Lotout C, Poujol M, Pitra P, Anczkiewicz R, Van Den Driessche J (2020) From burial to exhumation: emplacement and metamorphism of mafic eclogitic terranes constrained through multimethod petrochronology, case study from the Lévézou Massif (French Massif Central, Variscan Belt). J Petrol 61:egaa046.

Macaudière J, Marignac C, Weisbrod A (1987) Grandes nappes synschisteuses collisionnelles dans la catazone hercynienne des Cévennes médianes (Massif Central, France). CR Acad Sci 304:1195-1199.

Marcoux E, Pélisson P, Baudron JC, Lhégu J, Touray JC (1990) Ages des formations filoniennes à fluorine-barytine-quartz du district de Paulhaguet (Haute-Loire, Massif Central français). CR Acad Sci 311:829–835.

926 Marcoux E, Barré B, Pichavant M, Poujol M (2021) Âge et genèse de la coupole granitique à
927 métaux rares (Sn, Li, Nb-Ta, W) de Montebras (Creuse, Massif central français). BSGF -
928 Earth Sci Bull 192:16.
929 Marignac C, Leroy J, Macaudière J, Pichavant M, Weisbrod A (1980) Evolution
930 tectonométamorphique d'un segment de l'orogène hercynien : les Cévennes médianes,
931 Massif Central français. CR Acad Sci 291:605-608.
932 Marignac C, Cuney M (1999) Ore deposits of the French Massif Central: insight into the
933 metallogenesis of the Variscan collision belt. Miner Deposita 34:472-504.
934 Marignac C, Cuney M, Kesraoui M, Bouabsa L (2009) Differentiation-dedifferentiation
935 processes in the rare metal granite (RMG) lineages. In Williams P et al. (eds), Smart
936 Science for Exploration and Mining: Proceed 10th Biennial SGA Meeting, Townsville,
937 Australia 991-994.
938 Marignac C, Cuney M, Cathelineau M, Lecomte A, Carocci E, Pinto F (2020) The Panasqueira
939 Rare Metal Granite Suites and Their Involvement in the Genesis of the World-Class
940 Panasqueira W–Sn–Cu Vein Deposit: A Petrographic, Mineralogical, and Geochemical
941 Study. Minerals 10:562.
942 McDonough WF, Sun SS (1995) The composition of the Earth. Chem Geol 120:223–253.
943 Melleton J, Cocherie A, Faure M, Rossi P (2010) Precambrian protoliths and Early Paleozoic
944 magmatism in the French Massif Central: U–Pb data and the North Gondwana connection
945 in the west European Variscan belt. Gondwana Res 17:13–25.
946 Melleton J, Gloaguen E, Frei D (2015) Rare-elements (Li–Be–Ta–Sn– Nb) magmatism in the
947 European Variscan belt, a review. Proc 13th Biennial SGA Meeting Nancy 2:24–27.
948 Mialhe J (1980) Le massif granitique de la Borne: étude pétrographique, géochimique,
949 géochronologique et structurale. Unpublished Ph.D. thesis, Université de Clermont-
950 Ferrand, France, 170p.

951 Michaud JAS, Pichavant M (2019) The H/F ratio as an indicator of contrasted wolframite
952 deposition mechanisms. Ore Geol Rev 104:266-272.
953 Michaud JAS, Pichavant M (2020) Magmatic fractionation and the magmatic-hydrothermal
954 transition in rare metal granites: evidence from Argemela (Central Portugal). Geochim
955 Cosmochim Ac 289:130-157.
956 Michaud JAS, Gumiaux C, Pichavant M, Gloaguen E, Marcoux E (2020) From magmatic to
957 hydrothermal Sn-Li-(Nb-Ta-W) mineralization: the Argemela area (central Portugal). Ore
958 Geol Rev 116:103215.
959 Michaud JAS, Pichavant M, Villaros A (2021) Rare elements enrichment in crustal
960 peraluminous magmas: insights from partial melting experiments. Contrib Mineral Petr
961 176:1-33.
962 Monnier L, Salvi S, Melleton J, Bailly L, Béziat D, de Parseval P, Gouy S, Lach P (2019)
963 Multiple Generations of Wolframite Mineralization in the Echassieres District (Massif
964 Central, France). Minerals 9:637.
965 Monnier L, Salvi S, Jourdan V, Sall S, Bailly L, Melleton J, Béziat D (2020) Contrasting fluid
966 behavior during two styles of greisen alteration leading to distinct wolframite
967 mineralizations: The Echassières district (Massif Central, France). Ore Geol Rev
968 124:103648.
969 Monnier L, Salvi S, Melleton J, Lach P, Pochon A, Bailly L, Béziat D, De Parseval P (2022)
970 Mica trace-element signatures: Highlighting superimposed W-Sn mineralizations and fluid
971 sources. Chem Geol 600:120866.
972 Mougeot R, Respaut JP, Ledru P, Marignac C (1997) U-Pb chronology on accessory minerals
973 of the Velay anatectic dome (French Massif Central). Eur J Mineral 9:141-156.
974 Mourey Y (1985) Le leucogranite à topaze de Chavence. Un nouvel exemple de massif à Sn,
975 W, Li dans le Nord du Massif Central Français. CR Acad Sci 300:951–954.

976 Moyen JF, Laurent O, Chelle-Michou C, Couzinié S, Vanderhaeghe O, Zeh A, Villaros A,
977 Gardien V (2017) Collision vs. subduction-related magmatism: two contrasting ways of
978 granite formation and implications for crustal growth. Lithos 277:154-177.
979 Neymark LA, Holm-Denoma CS, Moscati RJ (2018) In situ LA-ICPMS U–Pb dating of
980 cassiterite without a known-age matrix-matched reference material: Examples from
981 worldwide tin deposits spanning the Proterozoic to the Tertiary. Chem Geol 483:410-425.
982 Noyé F (1985) Etude métallogénique des indices à étain-tungstène de Saint Mélany (Ardèche,
983 France). Unpublished Ph.D. thesis, Institut National Polytechnique de Lorraine, France,
984 285p.
985 Paton C, Hellstrom J, Paul B, Woodhead J, Hergt J (2011) Iolite: freeware for the visualization
986 and processing of mass spectrometric data. J Anal At Spectrom 26:2508–2518.
987 Pin C, Vielzeuf D (1983) Granulites and related rocks in Variscan median Europe: a dualistic
988 interpretation. Tectonophysics 93:47-74.
989 Raimbault L (1998) Composition of complex lepidolite-type granitic pegmatites and of
990 constituent columbite-tantalite, Chèdeville, Massif Central, France. Can Mineral 36:563–
991 583.
992 Raimbault L, Burnol L (1998) The Richemont rhyolite dyke, Massif Central, France: a
993 subvolcanic equivalent of rare metal granites. Can Mineral 36:265–282.
994 Raimbault L, Cuney M, Azencott C, Duthou JL, Joron JL (1995) Geochemical evidence for a
995 multistage magmatic genesis of Ta– Sn–Li mineralization in the granite at Beauvoir,
996 French Massif Central. Econ Geol 90:548–576.
997 Ramboz C, Schnapper D, Dubessy J (1985) The P-V-T-X-fO_2 evolution of H_2O-CO_2-CH_4-
998 bearing fluid in a wolframite vein: Reconstruction from fluid inclusion studies. Geochim
999 Cosmochim Ac 49:205-219.

1000 Renne PR, Swisher CC, Deino AL, Karner DB, Owens TL, DePaolo DJ (1998) Intercalibration
1001 of standards, absolute ages and uncertainties in $^{40}Ar/^{39}Ar$ dating. Chem Geol 145:117-152.
1002 Renne PR, Norman EB (2001) Determination of the half-life of ^{37}Ar by mass spectrometry.
1003 Phys Rev C 63:047302.
1004 Romer RL, Kroner U (2016) Phanerozoic tin and tungsten mineralization—tectonic controls
1005 on the distribution of enriched protoliths and heat sources for crustal melting. Gondwana
1006 Res 31:60–95.
1007 Rudnick RL, Gao S (2003) Composition of the Continental Crust. In Treatise on Geochemistry
1008 1st Edition (eds. HD Holland and KK Turekian) 3:1–64.
1009 Schmidt C, Romer RL, Wohlgemuth-Ueberwasser CC, Appelt O (2020) Partitioning of Sn and
1010 W between granitic melt and aqueous fluid. Ore Geol Rev 117:103263.
1011 Sizaret S, Marcoux E, Jébrak M, Touray JC (2004) The Rossignol fluorite vein, Chaillac,
1012 France: multiphase hydrothermal activity and intravein sedimentation. Econ Geol 99:1107-
1013 1122.
1014 Sizaret S, Marcoux E, Boyce A, Jébrak M, Stevenson R, Ellam R (2009) Isotopic (S, Sr, Sm/Nd,
1015 D, Pb) evidences for multiple sources in the Early Jurassic Chaillac F-Ba ore deposit (Indre,
1016 France). B Soc Geol Fr 180:83-94.
1017 Solé VA, Papillon E, Cotte M, Walter P, Susini JA (2007) A multiplatform code for the analysis
1018 of energy-dispersive X-ray fluorescence spectra. Spectrochim Acta B 62:63-68.
1019 Steiger RH, Jäger E (1977) Subcommission on geochronology: convention on the use of decay
1020 constants in geo- and cosmochronology. Earth Planet Sc Lett 36:359-362.
1021 Stipp M, Stuènitz H, Heilbronner R, Schmid SM (2002) The eastern Tonale fault zone: a
1022 'natural laboratory' for crystal plastic deformation of quartz over a temperature range from
1023 250 to 700°C. J Struct Geol 24:1861-1884.

1024 Talbot JY, Martelet G, Courrioux G, Chen Y, Faure M (2004) Emplacement in an extensional
1025 setting of the Mont Lozère–Borne granitic complex (SE France) inferred from
1026 comprehensive AMS, structural and gravity studies. J Struct Geol 26:11-28.
1027 Tapster S, Bright JW (2020) High-precision ID-TIMS cassiterite U–Pb systematics using a low-
1028 contamination hydrothermal decomposition: implications for LA-ICP-MS and ore deposit
1029 geochronology. Geochron 2:425-441.
1030 Tartèse R, Boulvais P (2010) Differentiation of peraluminous leucogranites “en route” to the
1031 surface. Lithos 114:353-368.
1032 Thierry J, Marignac C, Ledru P, Reboulet S, Dagain J, Naud G, Roger J, Laumonier B, Vernhet
1033 Y (2014) Evolution géologique de l’Ardèche crystalline. Notice explicative de la feuille
1034 Privas à 1/50 000, BRGM Edition, 99-131.
1035 Vallance J, Cathelineau M, Marignac C, Boiron MC, Fourcade S, Martineau F, Fabre C (2001)
1036 Microfracturing and fluid mixing in granites: W–(Sn) ore deposition at Vaulry (NW French
1037 Massif Central). Tectonophysics 336:43-61.
1038 Van Lichtervelde M, Salvi S, Beziat D, Linnen RL (2007) Textural features and chemical
1039 evolution in tantalum oxides: magmatic versus hydrothermal origins for Ta mineralization
1040 in the Tanco Lower pegmatite, Manitoba, Canada. Econ Geol 102:257–276.
1041 Van Lichtervelde M, Holtz F, Melcher F (2018) The effect of disequilibrium crystallization on
1042 Nb-Ta fractionation in pegmatites: Constraints from crystallization experiments of
1043 tantalite-tapiolite. Am Mineral 103:1401-1416.
1044 Villaros A, Laurent O, Couzinié S, Moyen JF, Mintrone M (2018) Plutons and domes: the
1045 consequences of anatectic magma extraction—example from the south-eastern French
1046 Massif Central. Int J Earth Sci 107:2819-2842.
1047 Villaseca C, Barbero L, Herreros V (1998) A re-examination of the typology of peraluminous
1048 granite types in intracontinental orogenic belts. Trans R Soc Edinb 89:113–119.

1049 Weisbrod A, Samama JC, Elmi S, Berger E, Feys R (1974) Carte géologique de France (1/50
1050 000), Feuille Largentière (864), BRGM, Orléans.
1051 Wolf M, Romer RL, Franz L, López-Moro FJ (2018) Tin in granitic melts: The role of melting
1052 temperature and protolith composition. Lithos 310:20-30.
1053 Wood SA, Samson IM (2000) The hydrothermal geochemistry of tungsten in granitoid
1054 environments: I. Relative solubilities of ferberite and scheelite as a function of T, P, pH,
1055 and mNaCl. Econ Geol 95:143-182.
1056 Woodhead JD, Hergt JM (2001) Strontium, neodymium and lead isotope analyses of NIST
1057 glass certified reference materials: SRM 610, 612, 614. Geostand Newslett 25:261–266.
1058 Wu M, Samson IM, Zhang D (2018) Textural features and chemical evolution in Ta–Nb oxides:
1059 implications for deuteric rare-metal mineralization in the Yichun granite-marginal
1060 pegmatite, Southeastern China. Econ Geol 113:937–960.
1061 Yang M, Yang YH, Wu ST, Romer RL, Che XD, Zhao ZF, Li WS, Yang JH, Wu FY, Xie LW,
1062 Huang C (2020) Accurate and precise in situ U–Pb isotope dating of wolframite series
1063 minerals via LA-SF-ICP-MS. J Anal Atom Spectrom 35:2191-2203.
1064 Yuan S, Williams-Jones AE, Romer RL, Zhao P, Mao J (2019) Protolith-related thermal
1065 controls on the decoupling of Sn and W in Sn-W metallogenic provinces: Insights from the
1066 Nanling region, China. Econ Geol 114:1005-1012.
1067 Zhao P, Chu X, Williams-Jones AE, Mao J, Yuan S (2022) The role of phyllosilicate partial
1068 melting in segregating tungsten and tin deposits in W-Sn metallogenic provinces. Geology
1069 50:121-125.
1070 Zhu ZY, Wang RC, Che XD, Zhu JC, Wei XL, Huang XE (2015) Magmatic–hydrothermal
1071 rare-element mineralization in the Song- shugang granite (northeastern Jiangxi, China):
1072 Insights from an electron-microprobe study of Nb–Ta–Zr minerals. Ore Geol Rev 65:749–
1073 760.

Figure captions

Fig. 1: Geological setting of the North Cévennes area in the southeastern French Massif Central (FMC). (a) Regional geologic map modified from Thierry et al. (2014) and Barbey et al. (2015) and based on the original map from Weisbrod et al. (1974), showing the location of wolframite vein occurrences (Serrecourte = SC, St-Mélany = SM). Major faults include: Ardèche Fault = AF, Beaume Fault = BF, Lignon Fault = LF, Pioule Fault = PF, and La Souche Fault = SF. The Metamorphic Mylonitic Vellave Zone (MMVZ) is from Bouilhol et al. (2006). (b) North-south cross-section showing the D3-D4 bending into large D3 upright folds and M3 isograde, as well as the Rocles granite laccolith. The M4 cordierite-bearing diatexites overprinted the D3-D4 structures and were in turn crosscut by the D5-related Tanargue late-orogenic granite. Map line of cross-section A-A' is shown on Fig. 1a.

Fig. 2: Field relationships of the St-Mélany vein system. (a) View of the mineralized quartz vein system hosted by cordierite-biotite-bearing mica schists. (b) Zoom on the cassiterite and wolframite mineralization located at the hanging wall of quartz veins. (c) Aplitic dike crosscutting a mineralized quartz vein and the host mica schists with an apparent normal displacement. (d) Lamprophyre dike crosscutting the mineralized quartz vein system and the host mica schists. (e) Late quartz ± barite vein with open-space geodic infill and crack-and-seal textures. Abbreviations: Ab = albite, Apl = aplite, Cst = cassiterite, Lph = lamprophyre, Mc = mica schist, Qtz = quartz, Wfm = wolframite.

Fig. 3: Structural features of the St-Mélany vein system. (a) Subhorizontal quartz (Qtz) vein dipping at low-angle in the mica schists (Mc). (b) Decimeter-thick subhorizontal quartz vein showing boudinage deformation. (c) Subvertical quartz vein crosscutting the regional foliation

in mica schists and offset by horizontal left-lateral fault. (d) Detailed view of quartz digitations in the mica schist. (e-f) Quartz veins deformed by asymmetric folds with axial planes subparallel to the foliation in mica schists.

Fig. 4: Paragenetic sequence of the St-Mélany mineralized veins incorporating new observations presented in this study and previous descriptions (Noyé 1985). Thick and thin lines correspond to relative mineral abundance.

Fig. 5: Mineralogical characteristics of the St-Mélany vein system. (a) Wolframite at the hanging wall of a subhorizontal quartz vein with minor scheelite. (b) Cluster of cassiterite at the hanging wall of a subhorizontal quartz vein with albite. (c) Coarse-grained muscovite fringe along a mineralized quartz vein. (d) Cassiterite and muscovite pod in the mica schists, close to a mineralized quartz vein. (e) Quartz-cassiterite-albite-beryl-muscovite assemblage in a mineralized vein. (f) Quartz-pyrite-chalcopyrite assemblage in a mineralized vein with dissolution vugs. Abbreviations: Ab = albite, Brl = beryl, Ccp = chalcopyrite, Cst = cassiterite, Mc = mica schist, Ms = muscovite, Py = pyrite, Qtz = quartz, Scl = scheelite, Wfm = wolframite.

Fig. 6: Photomicrographs of mineralized quartz veins from St-Mélany. (a) Quartz composing the vein showing intracrystalline deformation and dynamic recrystallization (cross-polarized light; sample ARD-14-03). (b) Coarse-grained muscovite fringe at the selvage of a mineralized quartz vein (cross-polarized light; sample ARD-13-12). (c) Cassiterite overgrown on coarse muscovite within a deformed quartz vein (cross-polarized light; sample ARD-13-77a). Note the intense deformation of quartz with development of a mylonitic foliation wrapping the cassiterite. (d) Wolframite and cassiterite within a deformed quartz vein cut by late quartz veinlets (cross-polarized light; sample ARD-14-01). (e) Scheelite that partially replaced

wolframite along microfractures and crystal borders (cross-polarized light; sample ARD-14-06). Note the undulose extinction of scheelite. (f) Subhedral scheelite partially corroded and cut by a pyrite-chalcopyrite assemblage in a mineralized quartz vein (plane-polarized light; sample ARD-13-18b). Abbreviations: Ccp = chalcopyrite, Cst = cassiterite, Ms = muscovite, Py = pyrite, Qtz = quartz, Scl = scheelite, Wfm = wolframite.

Fig. 7: Petrographic features of granitic dikes from St-Mélany. Representative rock sample (a) and cross-polarized photomicrograph (b) of aplitic dike composed of a fine-grained assemblage of quartz, albite, muscovite, and tourmaline (sample ARD-13-21). Representative rock sample (c) and cross-polarized photomicrograph (d) of pegmatitic dike composed of coarse-grained quartz, K-feldspar, plagioclase, and muscovite (sample ARD-13-72). Abbreviations: Ab = albite, Kfs = K-feldspar, Ms = muscovite, Qtz = quartz, Tur = tourmaline.

Fig. 8: Backscattered electron images (a-d) of columbite-tantalite and cassiterite in granitic pegmatite from St-Mélany (sample ARD-13-72). (a) Elongated grain of columbite-tantalite displaying a zoning composed of the succession of a dark core (i), dark rim-1 (ii), dark rim-2 (iii), light grey rim-3 (iv), dark rim-4 (v), and late overgrowth (vi). (b) Composite columbite-tantalite aggregate showing complex zoning and patchy texture. (c) Fe-tantalite grains (v) overgrown by Fe-tapiolite (vi). (d) Subhedral cassiterite (Cst) grain with minor overgrowths of Fe-tapiolite (vi). (e) Mn/(Fe+Mn) vs. Ta/(Ta+Nb) diagram showing the compositional variation of columbite-tantalite and the evolutionary trend (grey arrow).

Fig. 9: Whole rock compositions of granitic dikes from St-Mélany compared to the nearby Rocles and Borne granites. The compositions of mafic intrusive rocks (vaugnerite, lamprophyre) exposed in the North Cévennes area are shown for comparison. (a) Alumina

saturation diagram representing the molar ratios A/NK = $Al_2O_3/(Na_2O+K_2O)$ vs. A/CNK = $Al_2O_3/(CaO+Na_2O+K_2O)$. (b) B-A diagram showing the peraluminous index A = Al-(Na+K+2Ca) vs. the differentiation index B = Fe+Mg+Ti expressed in millications (Debon and Le Fort 1983; Villaseca et al. 1998). The subdivision of the peraluminous domain corresponds to low peraluminous (l-P), moderately peraluminous (m-P), highly peraluminous (h-P), and felsic peraluminous (f-P). (c-d) Multi-element diagram normalized by the upper continental crust (UCC) values of Rudnick and Gao (2003). (e-f) REE spider diagram normalized to CI chondrite values of McDonough and Sun (1995). Whole rock data for the granitoids and mafic rocks were compiled from Bellanger (1980), Mialhe (1980), Noyé (1985), Harlaux (2016), and Moyen et al. (2017). The grey field represents the compositional range of peraluminous rare metal granites and pegmatites from the French Massif Central (data from Aubert 1969; Mourey 1985; Cuney et al. 1992; Raimbault et al. 1995; Raimbault 1998; Raimbault and Burnol 1998; Harlaux et al. 2021; Marcoux et al. 2021).

Fig. 10: Tera-Wasserburg U-Pb diagrams for wolframite and cassiterite from St-Mélany analyzed by LA-ICP-MS. (a) Wolframite and cassiterite from a mineralized quartz vein (sample ARD-14-01). The enlarged panel showing the overlapping error ellipses of near-concordant data from cassiterite and wolframite is shown as inset. (b) Cassiterite from granitic pegmatite dikes crosscutting the St-Mélany vein system (samples ARD-13-22 and ARD-13-72). Data-point error ellipses and ages are shown at 2σ, with uncertainties into parentheses including the long-term excess variance. Rejected analyses are shown by grey ellipses. Colored lines correspond to linear regression through the data and the grey envelopes are the associated uncertainties.

Fig. 11: $^{40}Ar/^{39}Ar$ weighted mean age for muscovite from the selvage of a mineralized quartz vein from St-Mélany (sample ARD-13-12). All data and apparent ages are shown at 2σ uncertainty. The grey envelope correspond to the calculated weighted mean age with associated uncertainties.

Fig. 12: Schematic block diagrams summarizing the polyphase evolution of the St-Mélany vein system. (a) Development of regional penetrative foliation and syn-foliation quartz lenses in the Cévennes mica schists during the compressive D2 event (ca. 340-330 Ma). (b) Hydrofracturing and formation of the W-Sn-mineralized quartz veins during the compressive D3 event (ca. 320-310 Ma). (c) Emplacement of rare metal granitic dikes and lamprophyres crosscutting the mica schists and the mineralized quartz veins during the extensional D4 event (ca. 305-300 Ma).

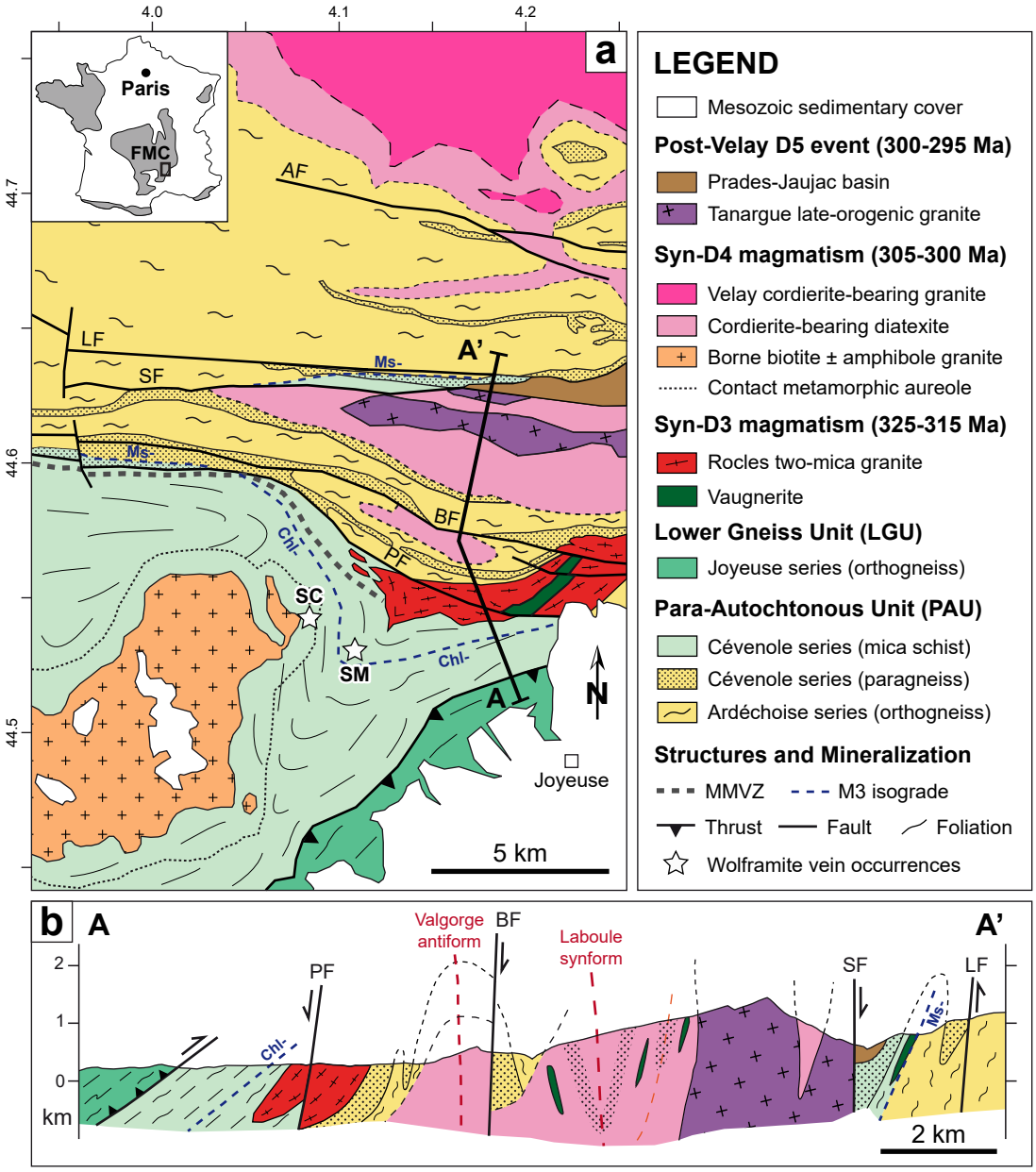
a
4.0
4.1
4.2
44.7
44.6
44.5
Paris
FMC
AF
LF
SF
Ms-
A'
A
BF
PF
Chl-
SC
SM
N
Joyeuse
5 km
LEGEND
Mesozoic sedimentary cover
Post-Velay D5 event (300-295 Ma)
Prades-Jaujac basin
Tanargue late-orogenic granite
Syn-D4 magmatism (305-300 Ma)
Velay cordierite-bearing granite
Cordierite-bearing diatexite
Borne biotite ± amphibole granite
Contact metamorphic aureole
Syn-D3 magmatism (325-315 Ma)
Rocles two-mica granite
Vaugnerite
Lower Gneiss Unit (LGU)
Joyeuse series (orthogneiss)
Para-Autochtonous Unit (PAU)
Cévenole series (mica schist)
Cévenole series (paragneiss)
Ardéchoise series (orthogneiss)
Structures and Mineralization
MMVZ
M3 isograde
Thrust
Fault
Foliation
Wolframite vein occurrences
b
A
A'
Valgorge antiform
BF
Laboule synform
PF
SF
LF
Chl-
Ms-
2
1
0
km
2 km

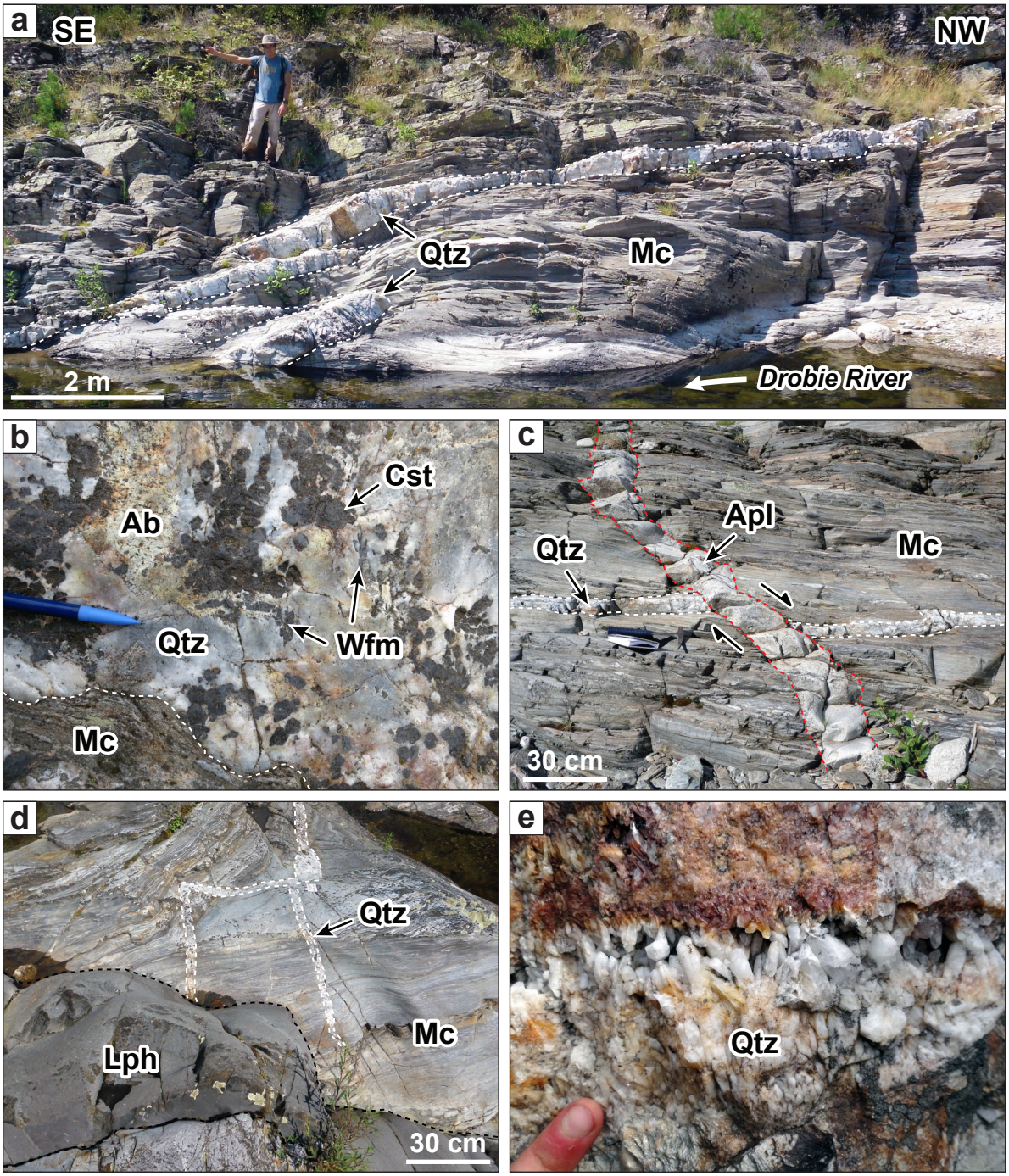
a
SE
NW
Qtz
Mc
2 m
Drobie River
b
Cst
Ab
Qtz
Wfm
Mc
c
Apl
Qtz
Mc
30 cm
d
Qtz
Mc
Lph
30 cm
e
Qtz

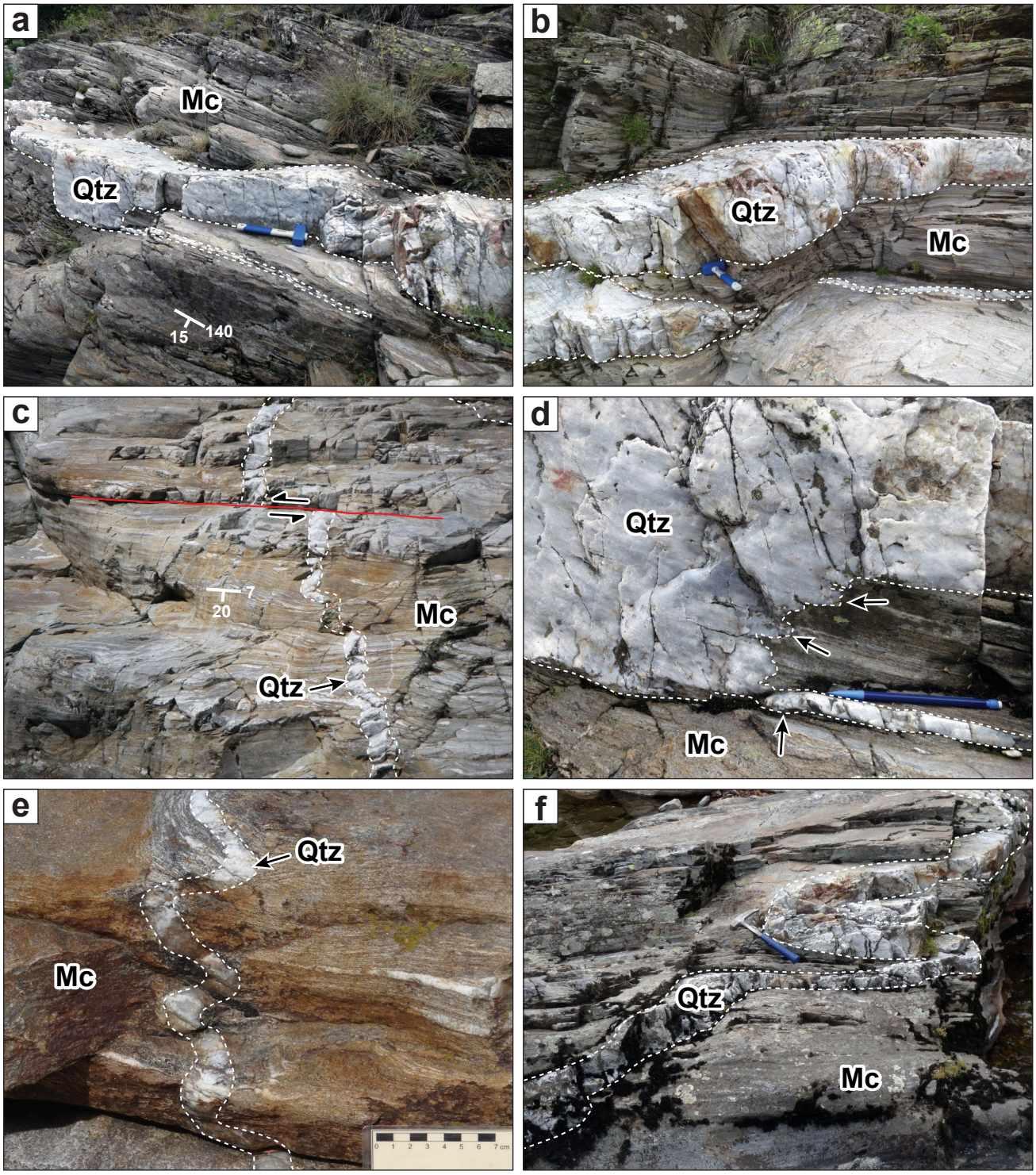
a
Mc
Qtz
15
140
b
Qtz
Mc
c
7
20
Mc
Qtz
d
Qtz
Mc
e
Qtz
Mc
f
Qtz
Mc

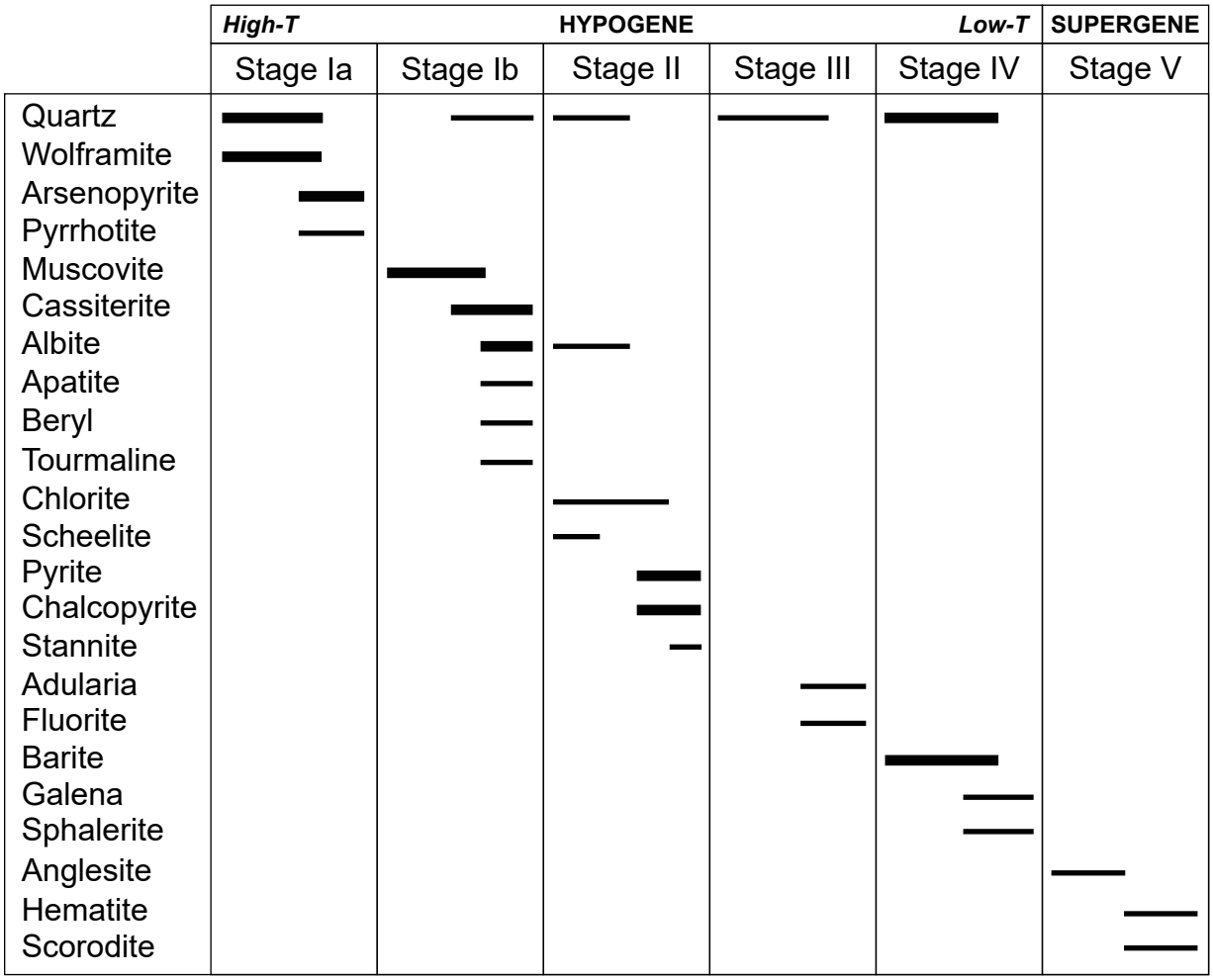
High-T
HYPOGENE
Low-T
SUPERGENE
Stage Ia
Stage Ib
Stage II
Stage III
Stage IV
Stage V
Quartz
Wolframite
Arsenopyrite
Pyrrhotite
Muscovite
Cassiterite
Albite
Apatite
Beryl
Tourmaline
Chlorite
Scheelite
Pyrite
Chalcopyrite
Stannite
Adularia
Fluorite
Barite
Galena
Sphalerite
Anglesite
Hematite
Scorodite

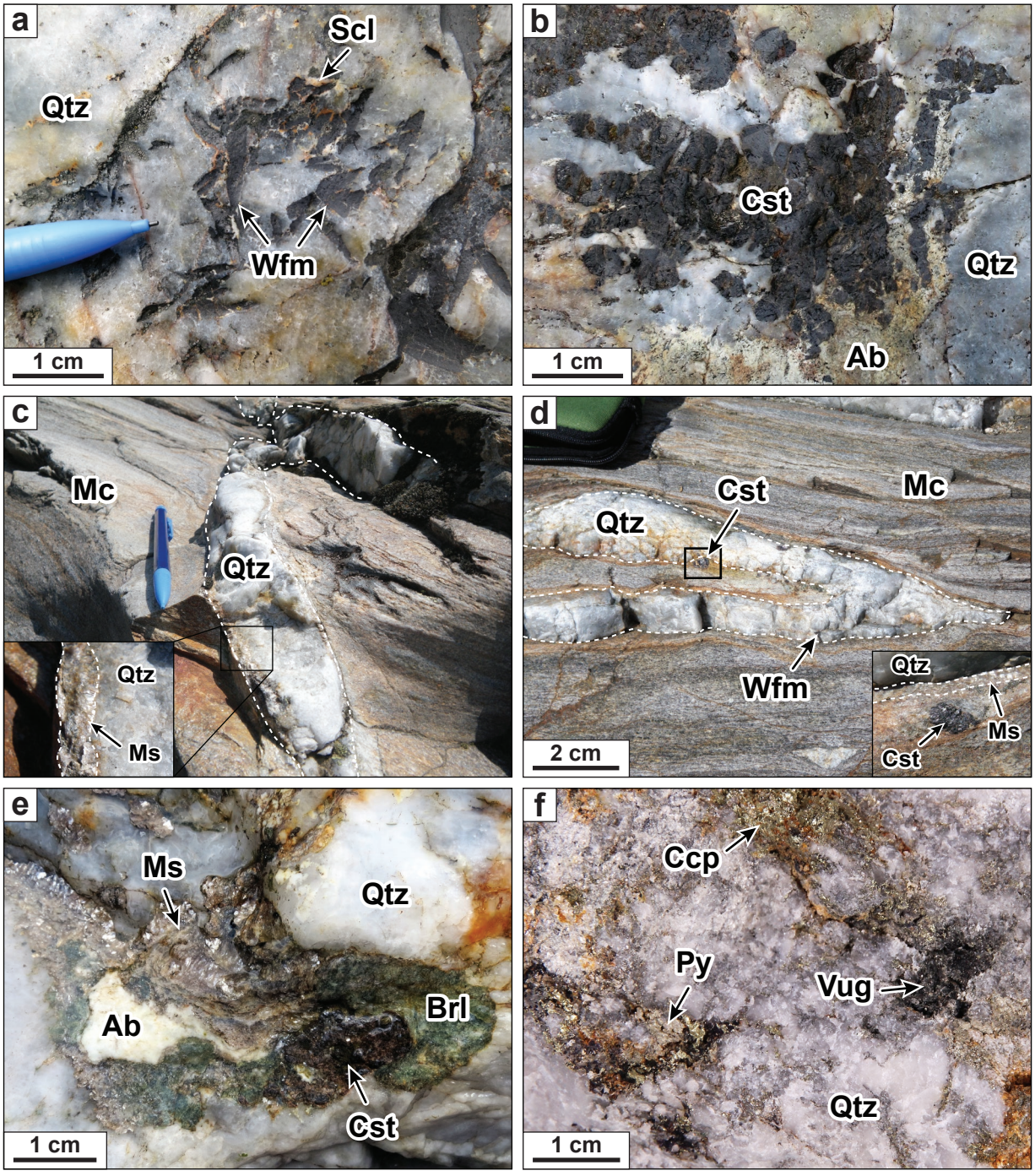
a
Scl
Qtz
Wfm
1 cm
b
Cst
Qtz
Ab
1 cm
c
Mc
Qtz
Qtz
Ms
d
Cst
Mc
Qtz
Wfm
Qtz
Ms
Cst
2 cm
e
Ms
Qtz
Brl
Ab
Cst
1 cm
f
Ccp
Py
Vug
Qtz
1 cm

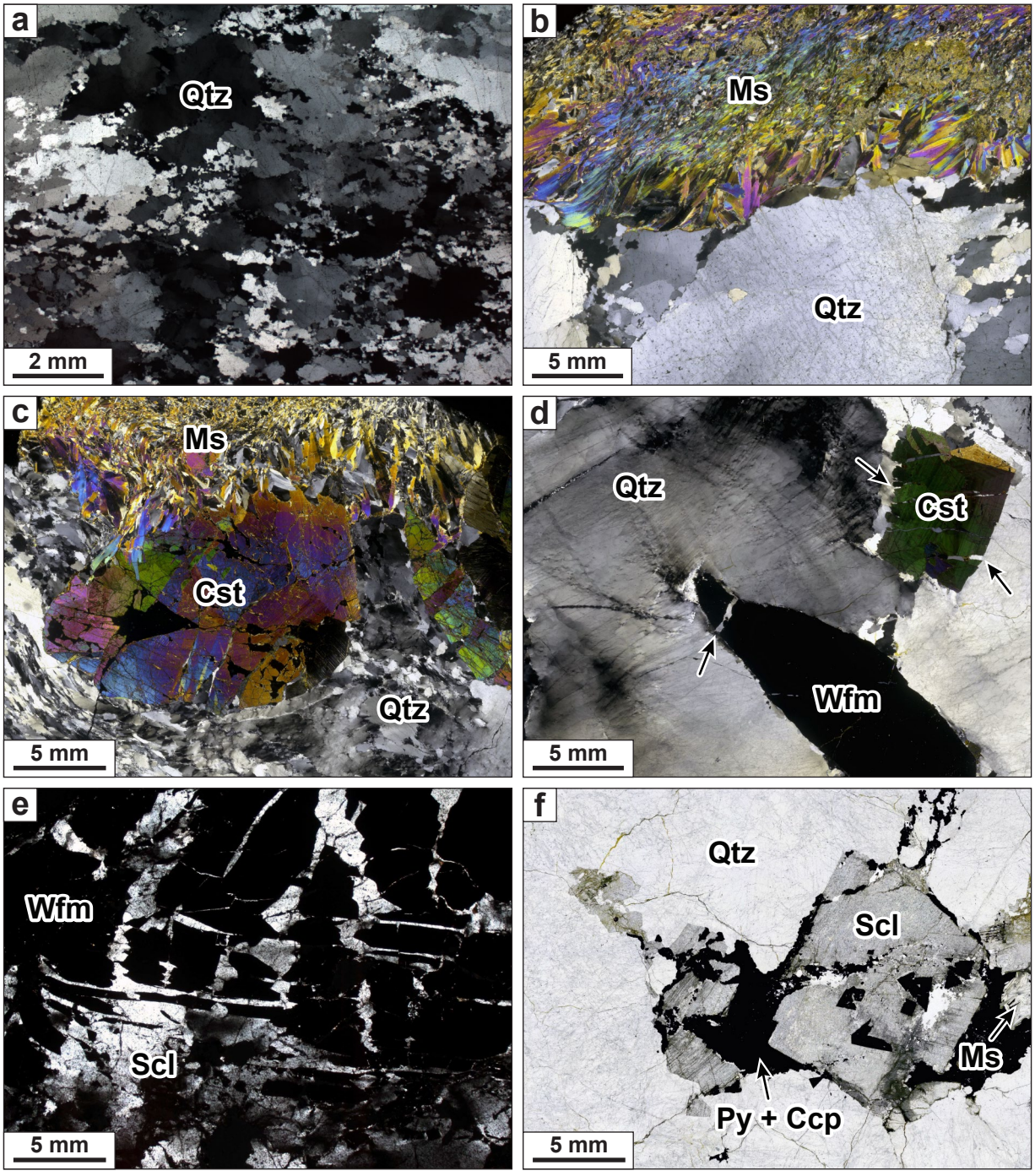
a
Qtz
2 mm
b
Ms
Qtz
5 mm
c
Ms
Cst
Qtz
5 mm
d
Qtz
Cst
Wfm
5 mm
e
Wfm
Scl
5 mm
f
Qtz
Scl
Ms
Py + Ccp
5 mm

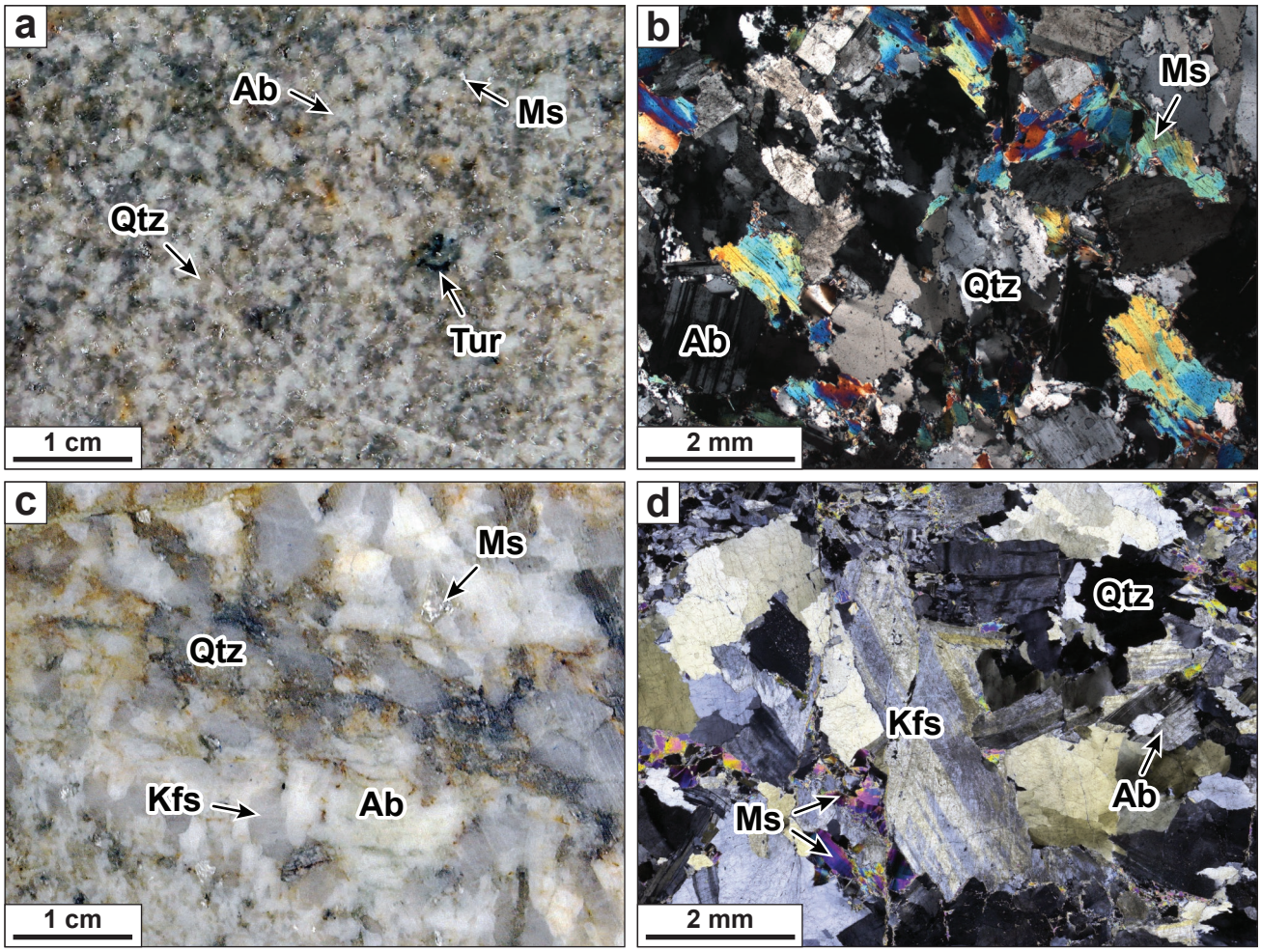
a
Ab
Ms
Qtz
Tur
1 cm
b
Ms
Qtz
Ab
2 mm
c
Ms
Qtz
Kfs
Ab
1 cm
d
Qtz
Kfs
Ab
Ms
2 mm

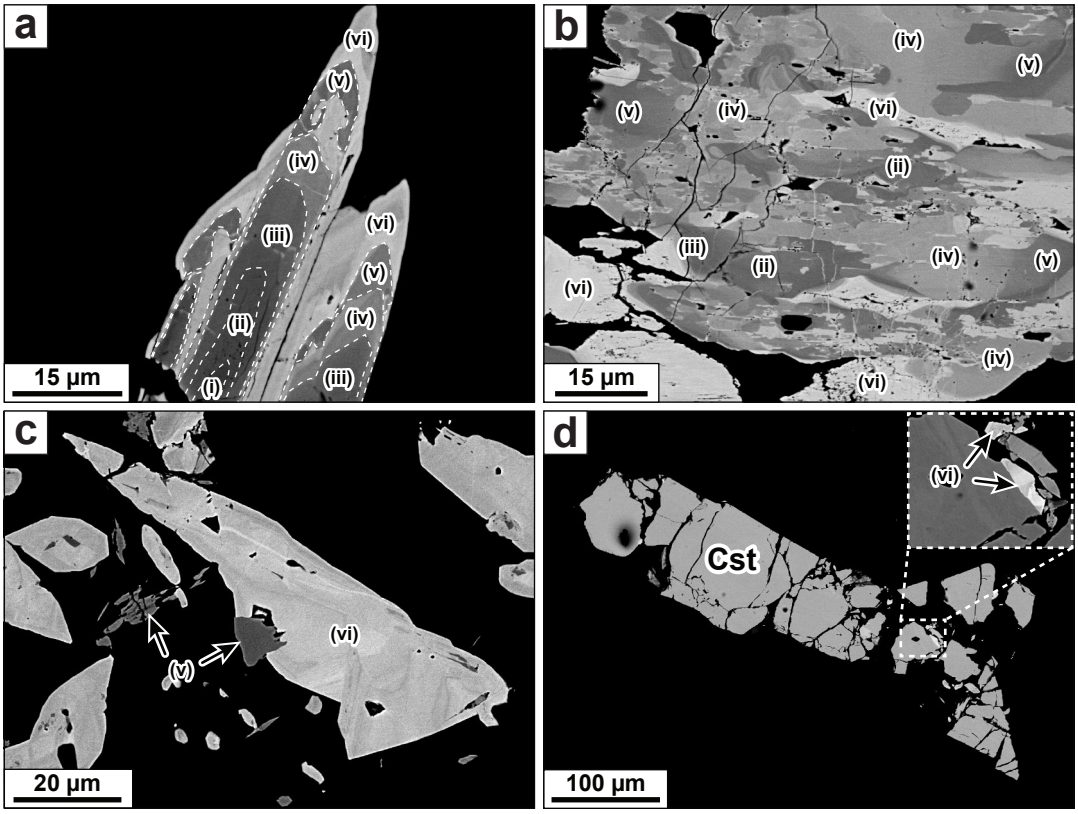
a
(vi)
(v)
(iv)
(iii)
(vi)
(v)
(ii)
(iv)
(i)
(iii)
15 µm
b
(iv)
(v)
(v)
(iv)
(vi)
(ii)
(iii)
(iv)
(v)
(ii)
(vi)
(iv)
(vi)
15 µm
c
(vi)
(v)
20 µm
d
(vi)
Cst
100 µm

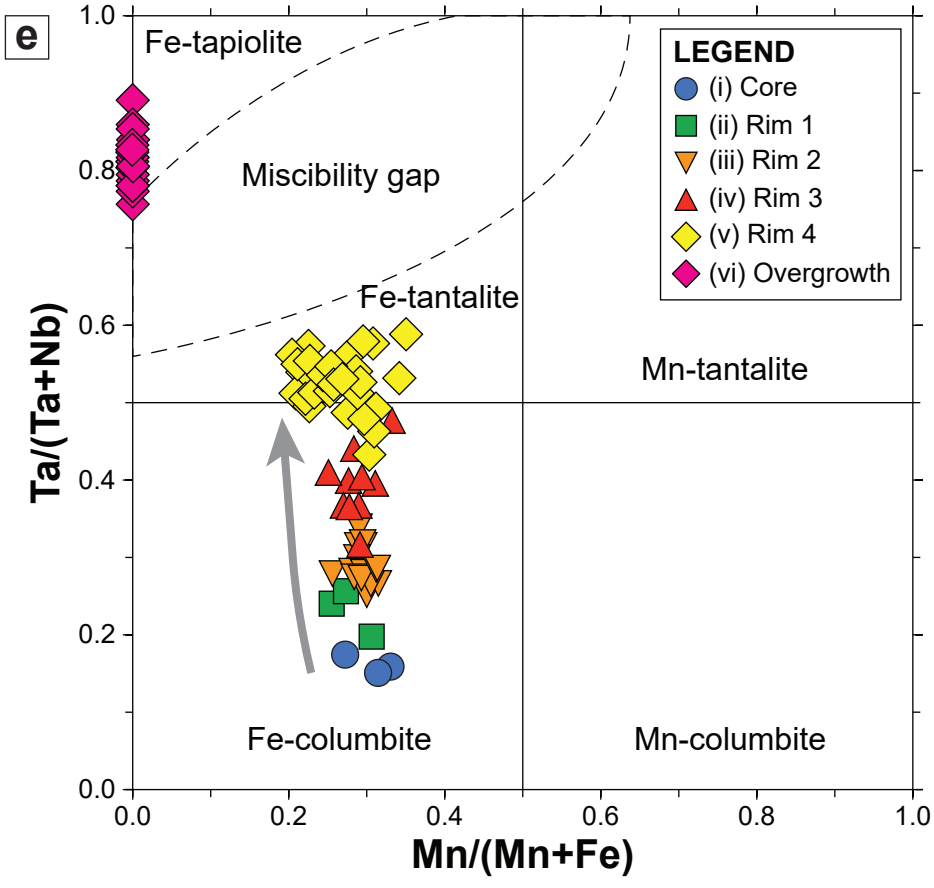
e
Fe-tapiolite
Miscibility gap
Fe-tantalite
Mn-tantalite
Fe-columbite
Mn-columbite
LEGEND
(i) Core
(ii) Rim 1
(iii) Rim 2
(iv) Rim 3
(v) Rim 4
(vi) Overgrowth
Ta/(Ta+Nb)
Mn/(Mn+Fe)
0.0
0.2
0.4
0.6
0.8
1.0

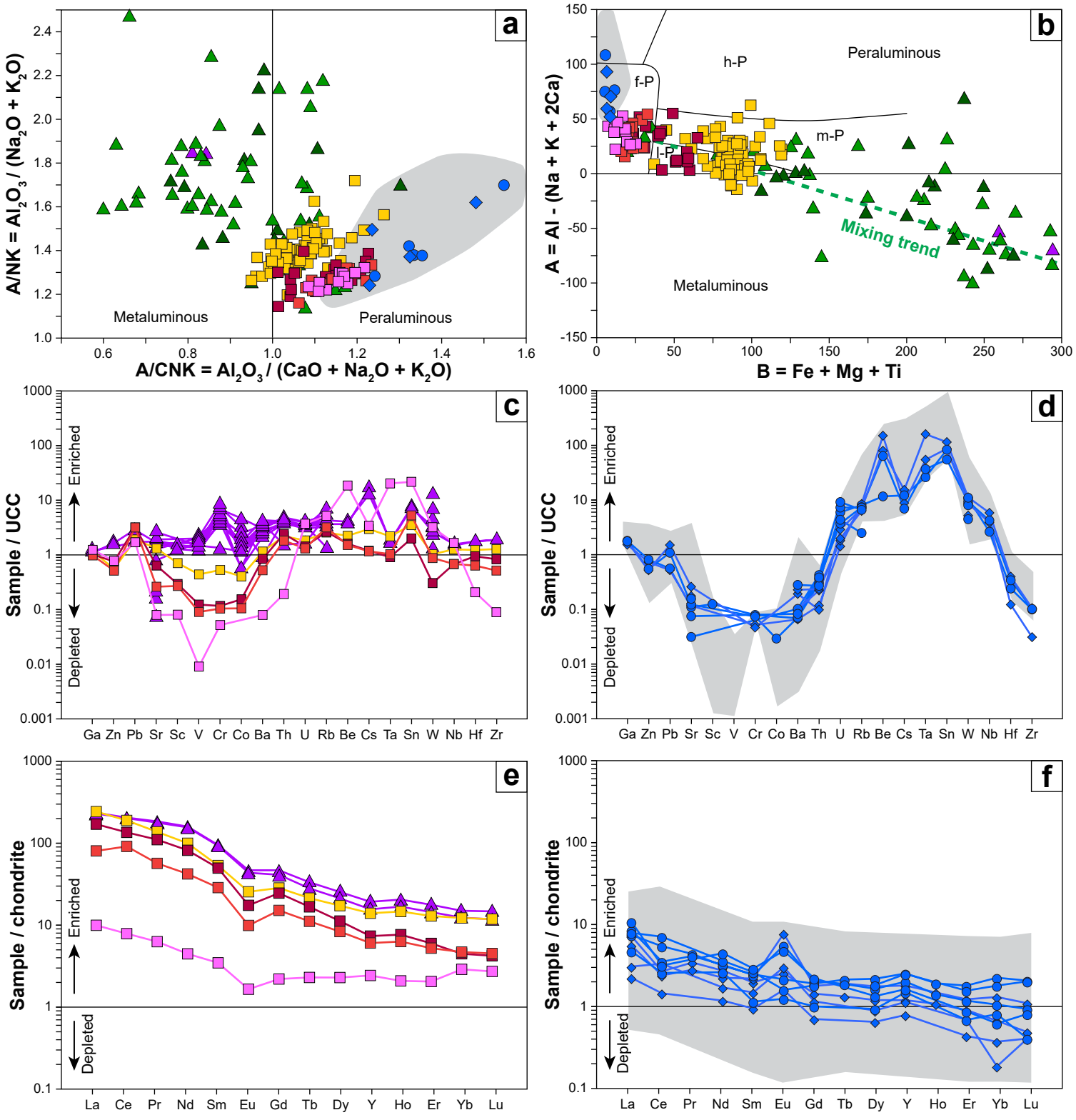
a
A/NK = Al2O3 / (Na2O + K2O)
A/CNK = Al2O3 / (CaO + Na2O + K2O)
Metaluminous
Peraluminous
b
A = Al - (Na + K + 2Ca)
B = Fe + Mg + Ti
h-P
f-P
m-P
l-P
Peraluminous
Metaluminous
Mixing trend
c
Sample / UCC
Enriched
Depleted
Ga Zn Pb Sr Sc V Cr Co Ba Th U Rb Be Cs Ta Sn W Nb Hf Zr
d
Sample / UCC
Enriched
Depleted
Ga Zn Pb Sr Sc V Cr Co Ba Th U Rb Be Cs Ta Sn W Nb Hf Zr
e
Sample / chondrite
Enriched
Depleted
La Ce Pr Nd Sm Eu Gd Tb Dy Y Ho Er Yb Lu
f
Sample / chondrite
Enriched
Depleted
La Ce Pr Nd Sm Eu Gd Tb Dy Y Ho Er Yb Lu
LEGEND
Rocles granite (ca. 325-315 Ma)
Muscovite-rich unit
Two-mica unit
Biotite-rich unit
Borne granite (ca. 305-300 Ma)
Megacrystic unit
St-Mélany granitic dikes (ca. 305 Ma)
Aplite
Pegmatite
Mafic intrusive rocks
Syn-M3 vaugnerite
Syn-M4 vaugnerite
St-Mélany lamprophyre

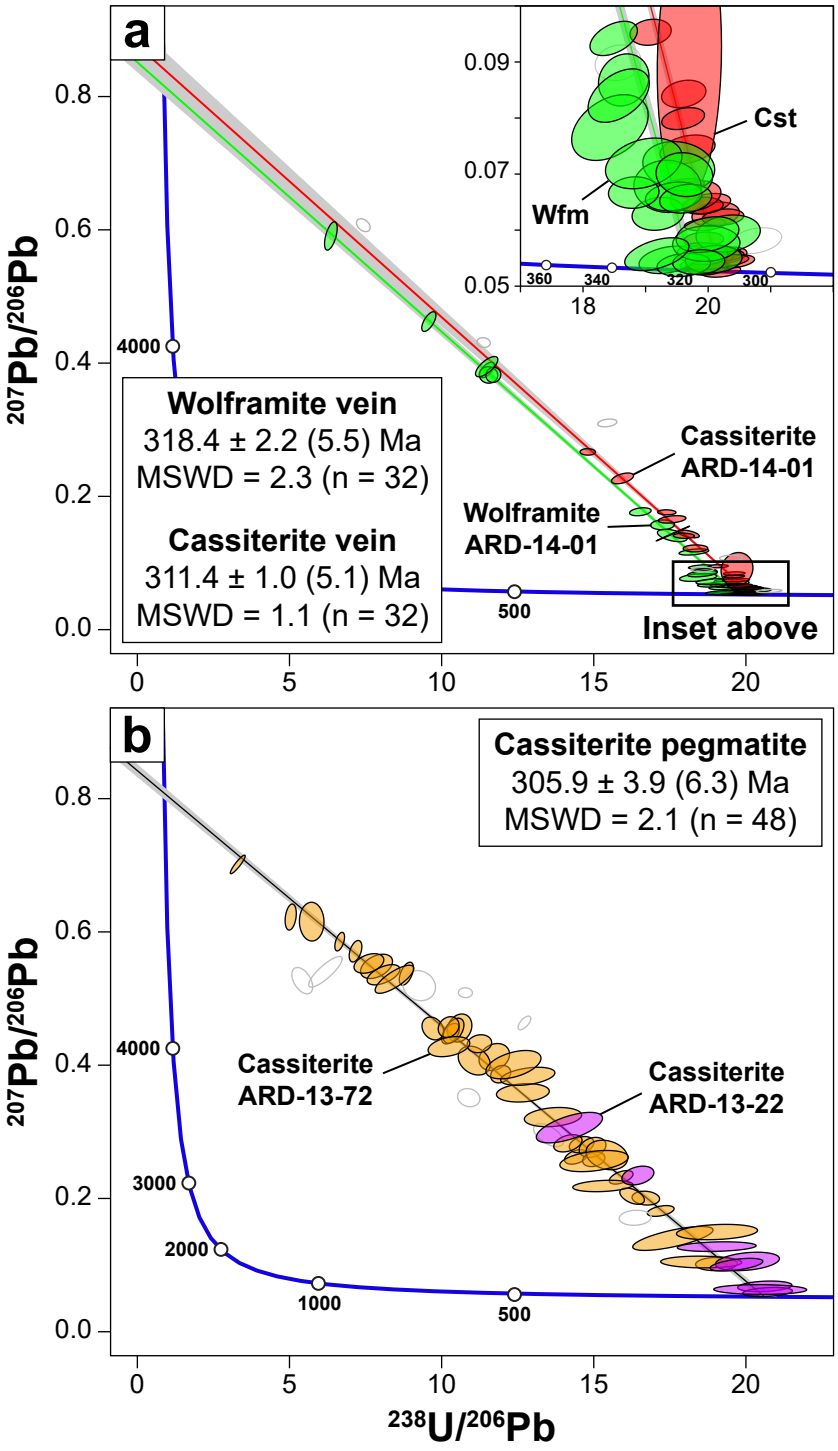
a
Wolframite vein
318.4 ± 2.2 (5.5) Ma
MSWD = 2.3 (n = 32)
Cassiterite vein
311.4 ± 1.0 (5.1) Ma
MSWD = 1.1 (n = 32)
Cassiterite
ARD-14-01
Wolframite
ARD-14-01
Inset above
Cst
Wfm
4000
500
b
Cassiterite pegmatite
305.9 ± 3.9 (6.3) Ma
MSWD = 2.1 (n = 48)
Cassiterite
ARD-13-72
Cassiterite
ARD-13-22
4000
3000
2000
1000
500
207Pb/206Pb
238U/206Pb

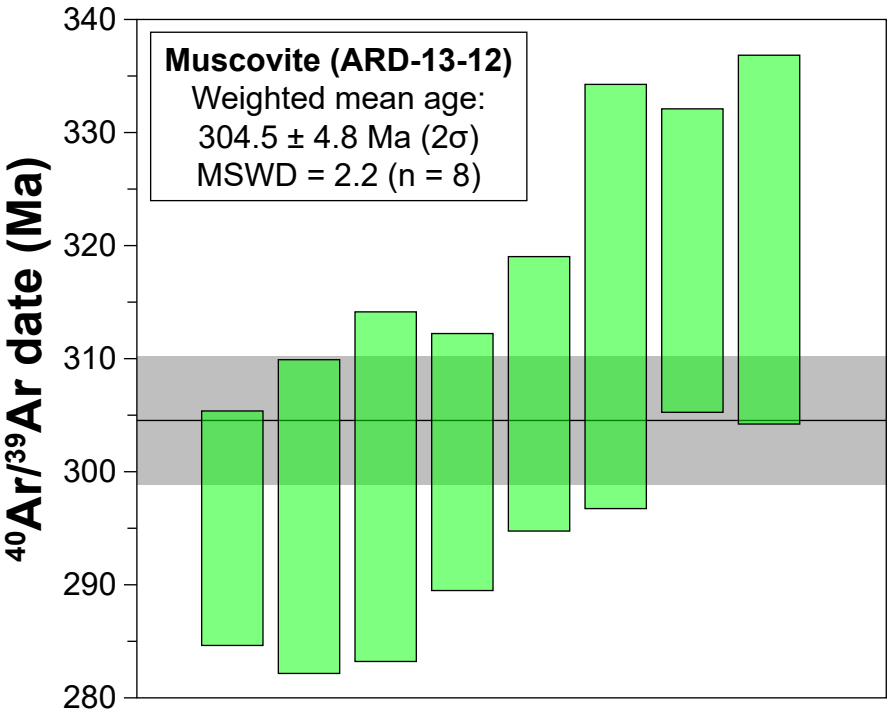
Muscovite (ARD-13-12)
Weighted mean age:
304.5 ± 4.8 Ma (2σ)
MSWD = 2.2 (n = 8)
340
330
320
310
300
290
280
40Ar/39Ar date (Ma)

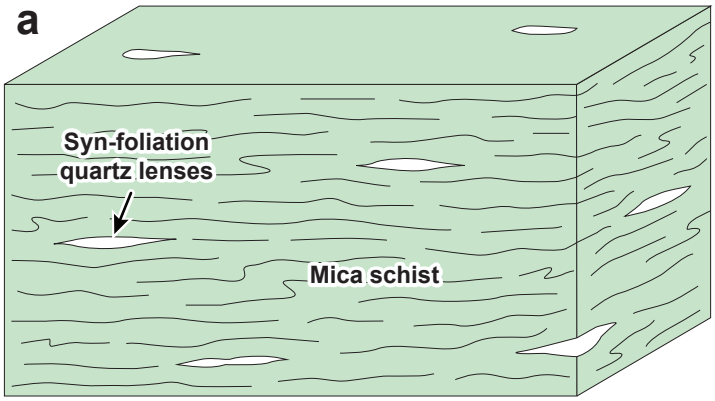

D2 event (ca. 340-330 Ma)

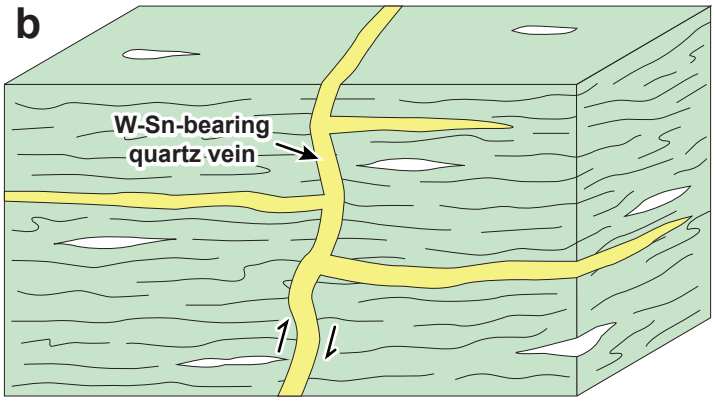

D3 event (ca. 320-310 Ma)

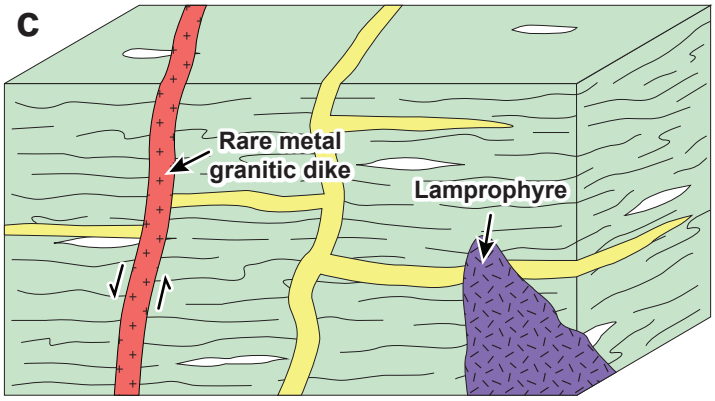

D4 event (ca. 305-300 Ma)